The cosmic X-ray and gamma-ray background from dark matter annihilation

Jesús Zavala,[1,2,*] Mark Vogelsberger,[3] Tracy R. Slatyer,[4] Abraham Loeb,[3] and Volker Springel[5,6]

[1]*Max-Planck-Institut für Astrophysik, Karl-Schwarzschild-Straße 1, 85740 Garching bei München, Germany*
[2]*Department of Physics and Astronomy, University of Waterloo, Waterloo, Ontario, N2L 3G1, Canada*[†]
[3]*Harvard-Smithsonian Center for Astrophysics, 60 Garden Street, Cambridge, MA 02138, USA*
[4]*School of Natural Sciences, Institute for Advanced Study, Princeton, NJ 08540, USA*
[5]*Heidelberg Institute for Theoretical Studies, Schloss-Wolfsbrunnenweg 35, 69118 Heidelberg, Germany*
[6]*Zentrum für Astronomie der Universität Heidelberg, Astronomisches Recheninstitut, Mönchhofstr. 12-14, 69120 Heidelberg, Germany*

The extragalactic background light (EBL) observed at multiple wavelengths is a promising tool to probe the nature of dark matter. This radiation might contain a significant contribution from gamma-rays produced promptly by dark matter particle annihilation in the many halos and subhalos within our past-light cone. Additionally, the electrons and positrons produced in the annihilation give energy to the cosmic microwave photons to populate the EBL with X-rays and gamma-rays. To study these signals, we create full-sky maps of the expected radiation from both of these contributions using the high-resolution Millennium-II simulation of cosmic structure formation. Our method also accounts for a possible enhancement of the annihilation rate by a Sommerfeld mechanism due to a Yukawa interaction between the dark matter particles prior to annihilation. We use upper limits on the contributions of unknown sources to the EBL to constrain the intrinsic properties of dark matter using a model-independent approach that can be employed as a template to test different particle physics models. These upper limits are based on observational measurements spanning eight orders of magnitude in energy (from soft X-rays measured by the CHANDRA satellite to gamma-rays measured by the *Fermi* satellite), and on expectations for the contributions from non-blazar active galactic nuclei, blazars and star forming galaxies. To exemplify this approach, we analyze a set of benchmark Sommerfeld-enhanced models that give the correct abundance of dark matter, satisfy constraints from the cosmic microwave background, and fit the cosmic ray spectra measured by PAMELA and *Fermi* without any contribution from local substructure. We find that these models are in conflict with the EBL constraints unless the contribution of unresolved substructure is small and the dark matter annihilation signal dominates the EBL. We conclude that provided the collisionless cold dark matter paradigm is accurate, even for conservative estimates of the contribution from unresolved substructure and astrophysical backgrounds, the EBL is *at least* as sensitive a probe of these types of scenarios as the cosmic microwave background. More generally, our results disfavor an explanation of the positron excess measured by the PAMELA satellite based only on dark matter annihilation in the smooth Galactic dark matter halo.

PACS numbers: 95.35.+d,95.85.Nv,95.85.Pw

I. INTRODUCTION

A broad class of particles known as Weakly Interacting Massive Particles (WIMPs), are the best studied and arguably the most favored candidates to be the primary component of cosmic dark matter. The most prominent example of such particles is the neutralino that arises naturally in supersymmetry (SUSY); for recent reviews on neutralino dark matter see [1, 2]. WIMPs can explain the observed abundance of dark matter in a natural way and because they behave as cold dark matter (CDM) they are also favored by the prevailing ΛCDM cosmology, which is the most successful model of structure formation to date. Furthermore, most WIMPs are particularly appealing because they offer a relatively high chance of detection in the near future, through: i) direct detection experiments on Earth looking for the recoil of ordinary matter by scattering of WIMPs, and ii) indirect searches that look for standard model particles produced in the annihilation of WIMPs.

A number of observations in recent years have highlighted anomalies that might be caused by dark matter annihilation. The excess of positrons in cosmic rays above 10 GeV reported by the PAMELA experiment [3] is one of these observations, and although other astrophysical sources, such as pulsars [4] and supernova remnants [5], could explain the signal, the possibility of dark matter annihilation remains attractive and has motivated a significant number of papers on the topic. It is however necessary to invoke large annihilation rates and specific annihilation channels to explain the anomalies with dark matter annihilation alone [6]. These rates are orders of magnitude larger than the ones obtained assuming the standard values for the annihilation cross section that give the correct relic density of dark matter. Due to their higher densities, substructures in the local dark matter distribution can boost the annihilation rates, but not to the required level [7]. The non-linear collapse of collisionless dark matter halos leads to the formation of caustics, which due to their high density could significantly increase the annihilation rate. However, this increase is actually much less significant than previously thought [8, 9]. In the inner parts of halos, it is essentially negligible and can not be invoked to explain the high annihilation rates required to explain the PAMELA measurements.

Alternatively, an elegant solution may lie in an enhancement of the annihilation cross section by a Sommerfeld mechanism produced by the mutual interaction between WIMPs prior to their annihilation [10–12]. This enhancement could

[†]Current affiliation
[*]CITA National Fellow; Electronic address: jzavalaf@uwaterloo.ca

easily be large enough to explain the anomalous excess of cosmic ray positrons.

The annihilation rate can however not be arbitrarily large either as it is constrained by different observables. For example, dark matter annihilation can ionize and heat the photon-baryon plasma at recombination, creating perturbations in the Cosmic Microwave Background (CMB) angular power spectrum [13–15]. It can also alter the relic abundance of dark matter significantly [16, 17], and produce important $\mu-$ and $y-$type distortions of the CMB [17, 18]. All these observables hence constrain the degree to which the Sommerfeld mechanism can enhance the cross section. Nevertheless, it is possible to satisfy all these constraints and at the same time explain the positron excess measured by PAMELA [19].

An additional set of observations with the potential to constrain the annihilation cross section can come from the analysis of the extragalactic background radiation at multiple wavelengths. The annihilation of WIMPs can manifest itself as a cosmic background radiation with gamma-ray photons being produced promptly in all extragalactic sources with high dark matter density [20–28]. This gamma-ray radiation is complemented towards lower energies by a diffuse extragalactic background in photons that were not produced directly in the annihilation but gained energy via inverse Compton scattering off the energetic electrons and positrons produced during the annihilation [29–31].

The data collected by several telescopes over the last decades have given us a measurement of the extragalactic radiation background from soft X-rays to hard gamma-rays (e.g. [32]). In this broad energy range, most of the radiation is expected to be produced by astrophysical mechanisms different from dark matter annihilation. This has been partially confirmed by accounting for the radiation of known sources and by estimating the contribution of an expected population of sources yet to be observed. This combined set of observations and expectations puts strong constraints on the contribution of dark matter annihilation, being specially stringent in the soft-X-ray regime where $\sim 90\%$ of the emission comes from X-ray point sources, mostly Active Galactic Nuclei (AGN) [33], and on the gamma-ray regime where blazars and star-forming galaxies are expected to contribute significantly to the background radiation, at the level of $\sim 70\%$ [34, 35].

The hypothetical background radiation coming from (or being up-scattered in) all dark matter halos and their subhalos within our past light cone has been studied by different authors in the past using analytic approaches to model cosmic structure formation. An approach based directly on high-resolution numerical simulations is however desirable since it more accurately captures the non-linear phase of the evolution, even though the simulation imposes a resolution limit for smallest structure. It is then possible to construct simulated sky-maps of the background radiation that give a more complete description of the signal. Such an approach was developed in [36] to analyze the extragalactic gamma-ray radiation produced in situ by annihilation using the state-of-the-art Millennium II simulation [37]. In this paper, we extend this approach to include the contribution from CMB photons scattered by the electrons and positrons produced during annihilation.

By using this approach we are also able to easily include a velocity-dependent annihilation cross section via a Sommerfeld mechanism. Typically, the enhancement is inversely proportional to the local velocity dispersion of dark matter particles. Since our method is based on average values of the annihilation rate inside halos and their subhalos, the Sommerfeld enhancement is simply given by the mean velocity dispersion in each halo (subhalo), which is available in the simulation and can be measured accurately.

The paper is organized as follows. In Section II, we outline the formalism to calculate the extragalactic background radiation coming from in situ and up-scattered photons. A description of the Sommerfeld enhancement model we used and its implementation is given in Section III. The observational upper limits and main results of our work on the cosmic background radiation are presented in Section IV. Finally we present a summary and conclusions in Section V.

II. ANNIHILATION RADIATION FORMALISM

Our goal is to analyze the cosmic dark matter annihilation background (CDMAB), or more specifically, the radiation produced by dark matter annihilation in all extragalactic sources integrated over all redshifts along the line-of-sight of a fiducial observer, located at $z = 0$, for all directions on its two-dimensional full sky. To this end, we first define the local photon emissivity:

$$\mathcal{E} = \frac{f_{\rm WIMP}}{2} E \rho_\chi(\vec{x})^2 S(\sigma_{\rm vel}(\vec{x})), \quad f_{\rm WIMP} = \frac{{\rm d}N}{{\rm d}E}\frac{\langle\sigma v\rangle_0}{m_\chi^2} \tag{1}$$

where m_χ and ρ_χ are the mass and density of WIMPs, $\langle\sigma v\rangle_0$ is the thermally averaged product of the constant s-wave annihilation cross section and the velocity in the absence of Sommerfeld enhancement, and ${\rm d}N/{\rm d}E$ is the differential photon yield per annihilation. The velocity dispersion dependent factor $S(\sigma_{\rm vel})$ boosts the value of $\langle\sigma v\rangle_0$ through a Sommerfeld mechanism (see section III). We note that for consistency, the value of $\langle\sigma v\rangle_0$ should also give the correct dark matter relic density.

The CDMAB is given by the specific intensity, the energy of photons received per unit area, time, solid angle and energy range:

$$I = \frac{1}{4\pi}\int \mathcal{E}(E_0(1+z), z)\frac{{\rm d}r}{(1+z)^4} e^{-\tau(E_0,z)}, \tag{2}$$

where the integral is over the whole line of sight, r is the comoving distance and E_0 is the photon energy measured by the observer at $z = 0$. Note that $\mathcal{E}$ is evaluated at the blue-shifted energy $(1+z)E_0$ along the line-of-sight to compensate for the cosmological redshifting. The exponential term with an effective optical depth $\tau(E_0, z)$ takes into account the absorption of photons by the matter and radiation field along the line-of-sight. The relevant processes of photon absorption and their treatment are described in Appendix B.

In this work, we focus on two different contributions to the differential photon yield per annihilation event ${\rm d}N/{\rm d}E$. In

the following, we describe these contributions that we refer to as *in situ* and *up-scattered* photons.

A. In situ photons

The in-situ photons are directly created due to the annihilation process. They are in the gamma-ray energy range and are produced by three mechanisms: (i) continuum emission following the decay of neutral pions produced during the hadronization of the primary annihilation products; (ii) monoenergetic lines for WIMP annihilation in two-body final states containing photons; (iii) internal bremsstrahlung when the final products of annihilation are charged, leading to the emission of an additional photon in the final state. Process (i) is dominant at most gamma-ray energies, but processes (ii) and (iii) produce distinctive spectral features intrinsic to the annihilation phenomenon. This in situ contribution to the CDMAB has been studied in detail before by different authors. In this work we follow the analysis of [36], extending their results to lower energies as described below.

B. Up-scattered photons

The up-scattered photons originate in differently produced background photons that gain energy due to their interactions with particles produced in the annihilation of dark matter. We concentrate exclusively on Inverse Compton (IC) scattering as the mechanism contributing to the up-scattering of these photons, and on the CMB as the main photon background. There are additional backgrounds, like stellar and infrared light, that are dominant close to galactic discs in the center of relatively massive halos. However, most of the CDMAB comes from the integrated effect of low mass halos and subhalos (see Appendix C). In these places, the stellar component is rather small and the mean number density of starlight and infrared photons is much lower than that of the CMB.

Electrons and positrons are the annihilation byproducts participating in the scattering. These particles are quite energetic and have therefore usually a large $\gamma = 1/\sqrt{1-(v/c)^2}$ factor. This implies that they can up-scatter low energy photons to significantly higher energies, because of the γ^2-dependence of the peak energy of up-scattered photons. In this process, CMB photons increase their energy into the X-ray and low gamma-ray regimes [29].

The differential electron (and positron) yield that is relevant for the IC up-scattering of the CMB photons is found by solving a diffusion equation that takes into account the diffusion and energy losses of these particles:

$$\frac{\partial}{\partial t}\frac{\mathrm{d}n_\mathrm{e}}{\mathrm{d}E_\mathrm{e}} = \nabla\left[D_\mathrm{e}\nabla\frac{\mathrm{d}n_\mathrm{e}}{\mathrm{d}E_\mathrm{e}}\right] + \frac{\partial}{\partial E_\mathrm{e}}\left[b_\mathrm{e}\frac{\mathrm{d}n_\mathrm{e}}{\mathrm{d}E_\mathrm{e}}\right] + Q_\mathrm{e}, \quad (3)$$

where $\mathrm{d}n_\mathrm{e}/\mathrm{d}E_\mathrm{e}$ is the equilibrium electron spectrum, $D_\mathrm{e} = D_\mathrm{e}(E_\mathrm{e},\vec{x})$ is the diffusion coefficient, $b_\mathrm{e} = b_\mathrm{e}(E_\mathrm{e},\vec{x})$ is the energy loss term and $Q_\mathrm{e} = Q_\mathrm{e}(E_\mathrm{e},\vec{x}) = \mathcal{E}_\mathrm{e}/E_\mathrm{e}$[77] is the source function. Spatial diffusion due to scattering on the inhomogeneities of the ambient magnetic field can be neglected. This is because spatial diffusion is only relevant at relatively small scales, within a few kpc of the center of dark matter halos [38]. However, we are interested in a cosmological background radiation where most of the signal in a given area in the sky comes from unresolved sources far away, where spatial diffusion is clearly irrelevant. In this case, the steady-state solution to Eq. (3) can be approximated by:

$$\begin{aligned}\frac{\mathrm{d}n_\mathrm{e}}{\mathrm{d}E}(E_\mathrm{e},z) &\approx \frac{1}{b_\mathrm{e}(E_\mathrm{e},z)}\int_{E_\mathrm{e}}^{m_\chi}\mathrm{d}E'_\mathrm{e}\,Q_\mathrm{e}(E_\mathrm{e},\vec{x}) \\ &= \frac{\langle\sigma v\rangle_0}{2}\left(\frac{\rho_\chi(\vec{x})}{m_\chi}\right)^2 S(\sigma_\mathrm{vel}(\vec{x}))\frac{\mathrm{d}\tilde{n}_\mathrm{e}}{\mathrm{d}E}(E_\mathrm{e},z). \quad (4)\end{aligned}$$

The energy loss rate, $b_\mathrm{e}(E_\mathrm{e},z)$, for electrons and positrons receives contributions from different interaction processes: IC scattering with ambient photons, synchrotron radiation in the ambient magnetic field, Coulomb scattering with free electrons, ionization of atoms and bremsstrahlung radiation in interactions with the ambient matter field. As we explain in Appendix A, among all these cooling processes we only consider the first one since it dominates the photon energy range we are ultimately interested in. The energy loss term in Eq. (4) is hence given by Eq. (A1).

We further assume that the electrons and positrons produced in the annihilation process lose energy and reach equilibrium instantaneously (in a cosmological time frame), scattering the CMB photons at the same redshift at which the annihilation takes place (e.g. [39]). These up-scattered photons have a differential photon spectrum given by:

$$\frac{\mathrm{d}N_\mathrm{IC}}{\mathrm{d}E}(E,z) = \int \mathrm{d}E_\mathrm{e}\,\frac{\mathrm{d}\tilde{n}_\mathrm{e}}{\mathrm{d}E}(E_\mathrm{e},z)\,\tilde{P}_\mathrm{IC}\left(E,E_\mathrm{e},z\right), \quad (5)$$

where the IC power per scattered photon energy is:

$$\tilde{P}_\mathrm{IC}\left(E,E_\mathrm{e},z\right) = c\int \mathrm{d}\tilde{E}\,n_\mathrm{CMB}(\tilde{E},z)\sigma_\mathrm{KN}(E,E_\mathrm{e},\tilde{E}). \quad (6)$$

Here, $n_\mathrm{CMB}(\tilde{E},z)\mathrm{d}\tilde{E}$ is the number density of CMB photons in the energy range $(\tilde{E},\tilde{E}+\mathrm{d}\tilde{E})$ at redshift z:

$$n_\mathrm{CMB}(\tilde{E},z)\mathrm{d}\tilde{E} = \frac{8\pi}{(hc)^3}\frac{\tilde{E}^2\mathrm{d}\tilde{E}}{\exp[\tilde{E}/(k_\mathrm{B}\,T_0(1+z))]-1}, \quad (7)$$

where $T_0 = 2.725$ K is the CMB temperature today, which increases with redshift like $(1+z)T_0$. Finally, σ_KN is the differential Klein-Nishina cross-section for IC scattering

$$\sigma_\mathrm{KN}(E,E_\mathrm{e},\tilde{E}) = \frac{3\sigma_\mathrm{T}}{4\tilde{E}}\left(\frac{m_\mathrm{e}c^2}{E_\mathrm{e}}\right)^2 G\left(q,\Gamma_\mathrm{e}\right), \quad (8)$$

where σ_T is the Thomson cross-section, m_e the electron mass, and

$$G\left(q,\Gamma_\mathrm{e}\right) = \left[2q\ln q + (1+2q)(1-q) + \frac{(\Gamma_\mathrm{e}q)^2(1-q)}{2\left(1+\Gamma_\mathrm{e}q\right)}\right], \quad (9)$$

with

$$\Gamma_\mathrm{e} = \frac{4\tilde{E}E_\mathrm{e}}{(m_\mathrm{e}c^2)^2}, \quad q = \frac{E}{\Gamma_\mathrm{e}\left(E_\mathrm{e}-E\right)}. \quad (10)$$

Note that the Klein-Nishina cross-section depends on the increased energy of the up-scattered photon E, the energy of the original CMB photon $\tilde{E}$, and on the energy $E_{\rm e}$ of the electron that does the IC scatter. The limits for the various integrals above are given by the kinematic constraint of the IC scattering requiring $1/[4(E_{\rm e}/(m_{\rm e}c^2))^2] < q < 1$.

III. SOMMERFELD ENHANCEMENT

We include in our analysis a scenario where the annihilation is enhanced by the Sommerfeld mechanism (e.g. [10–12, 40]), restricting it to the case where the interaction between WIMPs prior to annihilation is mediated by a scalar boson of mass m_ϕ through a Yukawa potential with coupling constant $\alpha_{\rm c}$ (e.g. [41]). This case encompasses the large majority of the models that are typically used in the literature to account for the Sommerfeld enhancement, including the most common of these where $S \propto 1/\sigma_{\rm vel}$ (the so-called "$1/v$" boost). Even in models with nearly-degenerate interacting states and/or multiple force carriers, while the details of the enhancement differ, the general features remain similar. The enhancement saturates at sufficiently low velocities due to the finite range of the Yukawa interaction. For certain combinations of $\alpha_{\rm c}$ and m_ϕ, resonances associated with zero-energy bound states appear [78]. Close to these resonances, the enhancement gets significantly larger for low velocities and scales as $1/\sigma_{\rm vel}^2$. In this case, the enhancement also saturates eventually due to the finite lifetime of the states. Regardless of the values of the parameters, the boost to the cross-section disappears for velocities comparable to the speed of light. This argument has often been invoked to infer that the dark matter relic density is unaffected by the Sommerfeld enhancement, but it has been shown recently that this assumption is not correct [17].

A detailed description of the Sommerfeld model studied here has been presented elsewhere (e.g. [12, 41]). For the purposes of this work, we follow the description of [17] and mention that the enhancement $S(\sigma_{\rm vel})$ to the s-wave contribution to the annihilation rate is given by:

$$\langle\sigma v\rangle = \langle\sigma v\rangle_0 S(\sigma_{\rm vel}),$$
$$S(\sigma_{\rm vel}) = \left(\frac{1}{2\sigma_{\rm vel}^3\sqrt{\pi}}\int_0^1 S(\beta)\beta^2 e^{-\beta^2/4\sigma_{\rm vel}^2}\,{\rm d}\beta\right), \quad (11)$$

where $\beta = v_{\rm rel}/c$ is the relative velocity between the annihilating pair[79].

For definiteness, we choose two sets of parameters that fall within currently favored regions of the parameter space (e.g. [41]): case i) off-resonance: $m_\phi/m_\chi = 5\times10^{-4}$, $\alpha_{\rm c} = 3\times10^{-2}$ and case ii) near-resonance: $m_\phi/m_\chi = 2.98\times10^{-4}$, $\alpha_{\rm c} = 3\times10^{-2}$. The former is representative of the standard "$1/v$" boost with a maximum enhancement $S_{\rm max}\sim2000$ for $\sigma_{\rm vel,max}\sim10^{-5}$. The latter is a typical resonance case with $S\propto1/\sigma_{\rm vel}$ at intermediate velocities and $S\propto1/\sigma_{\rm vel}^2$ at low velocities up to a saturation $S_{\rm max}\sim10^6$ for $\sigma_{\rm vel,max}\sim6\times10^{-7}$.

By solving the Schrödinger equation for s-wave annihilation in the non-relativistic limit, we obtain $S(\beta)$ for the two cases chosen above, and use Eq. (11) to get the average annihilation boost $S(\sigma_{\rm vel})$ for each halo. Since we can estimate the change on the values of $S_{\rm max}$ and $\sigma_{\rm vel,max}$ for a different set of parameters, the results we obtain later using these representative cases serve us to analyze the whole range of possibilities that are expected for a Sommerfeld mechanism produced by a Yukawa potential.

The Sommerfeld enhancement alters the relic density of dark matter [16, 17]. During freeze-out, while the Sommerfeld enhancement is generally $\mathcal{O}(1)$, it is not negligible and can consequently have an $\mathcal{O}(1)$ effect on the relic density (requiring a reduction of the underlying annihilation cross section to compensate). After kinetic decoupling of the dark matter from the radiation bath, the typical velocities of the dark matter particles decrease rapidly: even for non-resonant (but unsaturated) enhancement, the enhanced annihilation rate keeps pace with the universe's expansion, and for resonant enhancement the dark matter annihilations can actually *recouple* (depending on the relative temperatures of freeze-out, kinetic decoupling and saturation of the enhancement), greatly reducing the relic density. Once the enhancement saturates, the annihilation rate no longer keeps pace with the expansion rate, and the comoving density of dark matter remains fixed. In all cases there is a significant effect on the relic density, and in order to produce the correct abundance today, the value of the annihilation cross-section before the onset of the enhancement needs to be smaller than for the case without Sommerfeld enhancement.

This result is relevant because it implies that any particle physics model without enhancement chosen to satisfy the observational bounds on the abundance of dark matter needs to be revised once the enhancement is included to test whether or not it still gives the correct relic density. The fully consistent way to do so is to incorporate the Sommerfeld enhancement into a Boltzmann code and re-sample the parameter space of that particular model to find allowed regions. Here, we follow a simpler approach. According to [17], the value of $\langle\sigma v\rangle_0$ should be lower by a factor between 1 and 10 compared to the case without enhancement in order to get the correct relic density. The precise reduction factor, f_Ω, depends on the intensity of the enhancement: $f_\Omega\sim0.1$ near resonances and $f_\Omega\sim0.5$ off-resonance. Therefore, by multiplying $\langle\sigma v\rangle_0$ by the corresponding f_Ω factor, we roughly take into account the effect on the relic density. In this way, a model without enhancement that gives the correct relic density with $\langle\sigma v\rangle_0$ will also give the right relic abundance with Sommerfeld enhancement, provided its annihilation cross section in the early Universe is chosen to be $f_\Omega\langle\sigma v\rangle_0$.

IV. EXTRAGALACTIC CDMAB

The procedure we follow to construct the simulated sky maps of the contribution of dark matter annihilation to the X-ray and gamma-ray extragalactic background radiation is essentially an extension of the one discussed in [36]. For a detailed description of the map-making technique we used, we hence refer the reader to section 5.1 of that paper.

According to Eq. (1), the local annihilation rate depends on the square of the local density of dark matter. For the computation of the cosmological background from an N-body simulation, it is more reliable to use analytically integrated quantities over whole dark matter halos (based on scaling laws tested with extremely high-resolution simulations of MW-like halos [42]) instead of trying to use individual simulation particles directly, which are subject to stronger resolution effects and numerical noise [36]. Using this method, each pixel in our sky maps receives contributions of all intervening resolved halos and subhalos along its corresponding past light cone. Additionally, we add the expected contribution of unresolved structures down to the damping scale limit of WIMPs ($10^{-6}\mathrm{M}_{\odot}$, see sections 5.2-5.4 of [36]). Since we are exploring the case with Sommerfeld enhancement in this paper, the formulae given in [36] need to be altered accordingly. In Appendix C we describe how we accomplish this.

The signal depends of course on the value of the photon yield $\mathrm{d}N/\mathrm{d}E$ as well, which contains contributions from in situ and up-scattered photons. These are determined by the intrinsic properties of WIMPs. As an example, we take a neutralino with a main annihilation channel into $b\bar{b}$. In particular, we use a benchmark point within the minimal supergravity (mSUGRA) framework (model L in Table I of [36]). This benchmark point has $m_{\chi} \sim 185$ GeV with annihilation into $b\bar{b}$ with a 99% branching ratio, and $\langle \sigma v \rangle \sim 6.2 \times 10^{-27}\mathrm{cm}^3\mathrm{s}^{-1}$. It belongs to the so-called "bulk region" within the mSUGRA 5-dimensional parameter space that is consistent with current constraints on the relic density of neutralinos (if neutralinos make up for all the observationally inferred dark matter density). We obtain the photon, electron and positron yields for this model using the numerical code DarkSUSY [43, 44] with the interface ISAJET [45].

In Fig. 1, we show the final photon yield spectrum for dark matter annihilation in the X-ray and gamma-ray energy range for the example just described. The contributions from in situ and up-scattered CMB photons are shown with solid red and blue lines, respectively. For reference, the in situ and equilibrium electron (positron) yields from annihilation are shown with dashed red and green lines, respectively [80]. The main bump and secondary peak that are clearly shown for the in situ photons correspond to the two main mechanisms mentioned in section II A, neutral pion decay and internal bremsstrahlung, respectively. The figure shows clearly that although in this case the largest photon yield is in the gamma-ray regime, there is a significant amount of X-ray radiation produced by IC scatter of the CMB photons. The contribution from up-scattered CMB photons is the dominant feature for other particle physics models. As an example of this we show in Fig.1 the total photon yield for one of a set of benchmark models that we use later in section IV C. The shape and normalization for this benchmark model 1 (see Table 1) are representative of all the benchmark models we will use.

Fig. 2 shows the contribution from dark matter annihilation to the X-ray and gamma-ray extragalactic background radiation for the particular SUSY model described above. The case without Sommerfeld enhancement is shown within the light-gray shaded region. This region is bracketed by the maximum and minimum values of the extrapolation for unresolved subhalos, which encompasses the astrophysical uncertainties in the contribution by low-mass subhalos that can not be resolved by the Millennium II simulation (see Appendix C). The medium-gray and dark-gray shaded regions are for the cases with Sommerfeld enhancement, off- and near-resonance, respectively.

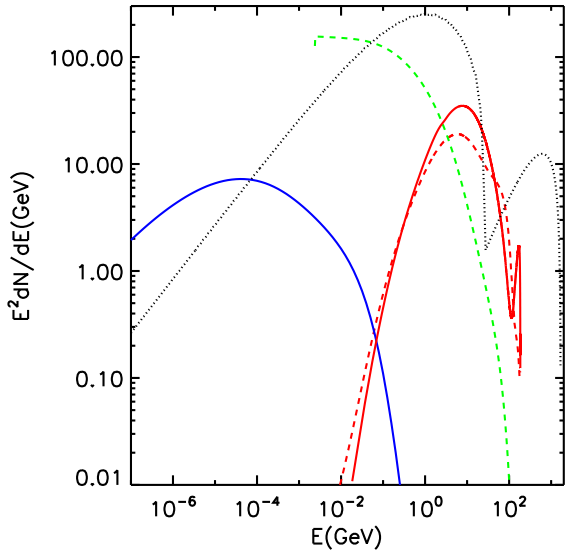

FIG. 1: Photon yield for dark matter annihilation in the X-ray and gamma-ray energy range for a ~ 185 GeV neutralino annihilating into $b\bar{b}$. The contributions from in-situ and up-scattered CMB photons are shown with solid red and blue lines, respectively. For reference, the in-situ and equilibrium electron yields from annihilation are shown with dashed red and green lines respectively (the equilibrium spectrum as defined in Eq. (4) was scaled by a factor of 10^{-16} to show it in the same figure). Also shown in the figure with a black dotted line is the total photon yield from benchmark model 1 of Table 1, see section IV C.

According to Fig. 2, any model with a photon yield similar to the one we used as an example (see Fig. 1), and with a mass ~ 200 GeV and $\langle \sigma v_0 \rangle \sim 6 \times 10^{-27}\mathrm{cm}^3\mathrm{s}^{-1}$, could be ruled out, depending on how relevant the contribution from unresolved halos and subhalos is. Any significant Sommerfeld enhancement is clearly ruled out by absolute measurements of the background in this case.

It is important to note that the Sommerfeld mechanism is of relevance for neutralinos only for masses $\gtrsim$TeV in the case of a minimal SUSY model like mSUGRA (e.g. [12, 40]). In this case, the force carriers responsible for the enhancement are the W and Z gauge bosons [81]. Therefore, boosts of order ~ 1000 or even larger are only possible for neutralinos with much higher masses than the model we have chosen as an example in Figs. 1 and 2. The net effect of a higher neutralino mass in the input photon and positron (electron) spectra is a shift of the X-ray and gamma-ray peaks shown in these figures towards higher energies. Nevertheless, the $\mathrm{d}N/\mathrm{d}E$ spectrum shown in Fig. 1 is generic for any model with a WIMP an-

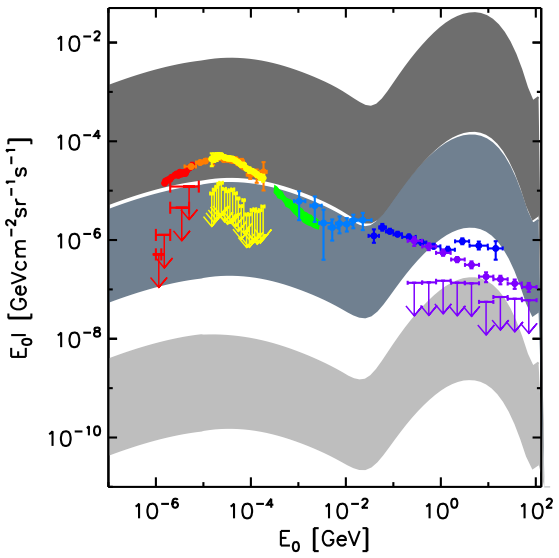

FIG. 2: CDMAB spectrum including in-situ and up-scattered CMB photons (gamma-rays from annihilation and CMB photons up-scattered to X-ray energies by electrons and positrons of the annihilation) for the cases of no-enhancement (light-gray), enhancement away from a resonance (medium-gray) and near a resonance (dark-gray). The upper and lower limits of each stripe bracket the uncertainty in the extrapolation of unresolved subhalos in the simulation. All cases are for a model with annihilation mainly into $b\bar{b}$, $m_\chi \sim 185$ GeV and $\langle\sigma v\rangle_0 \sim 6.2\times10^{-27}\mathrm{cm}^3\mathrm{s}^{-1}$. They all give approximately the correct relic density. Observations from soft X-rays to gamma-rays are marked with red to violet, following approximately a rainbow color pattern: red symbols [46], red arrows (Chandra, [33]), orange symbols (INTEGRAL, [47]), yellow symbols (SWIFT BAT, [32]), yellow arrows [48], green area (SMM, [49]), light blue (COMPTEL, [50]), blue (EGRET, [51]), violet (*Fermi-LAT*, [52]), violet arrows [34, 35]. The points with error bars are absolute measurements with 2σ or 1σ errors. The arrows pointing downwards are best estimate upper limits of the unresolved component of the signal, that is, the signal that can not be accounted for by already known or expected sources.

nihilating mainly into $b\bar{b}$. If such a generic model allows the inclusion of a new scalar boson responsible of the Sommerfeld enhancement, then the formalism described in Section III is applicable and Fig. 2 shows the expected level of enhancement of the CDMAB due to this mechanism.

The symbols shown in Fig. 2 represent inferences for the extragalactic X-ray and gamma-ray background radiation based on observational data as described in the following.

A. Observations

We are interested in measurements of the cosmic background radiation in an energy range going from soft X-rays to gamma-rays: $0.1\ \mathrm{keV} \leq E_0 \lesssim 100\ \mathrm{GeV}$. Because for $E_0 < 1$ keV the signal is completely dominated by galactic and local emission that varies with time and position, estimates of the extragalactic emission at these energies have not been possible [33, 53]. In the range $1\ \mathrm{keV} \leq E_0 \leq 200\ \mathrm{keV}$, the extragalactic X-ray background has been studied in detail by satellites such as CHANDRA, SWIFT and INTEGRAL. We take the absolute measurements obtained using the latter two satellites according to the analysis of [46] (red symbols in Fig. 2), [47] (orange symbols) and [32] (yellow symbols). At intermediate energies, $300\ \mathrm{keV} \leq E_0 \leq 30\ \mathrm{MeV}$, the measurements come from the Solar Maximum Mission (SMM) [49] and COMPTEL [50]. These measurements are shown with green and light blue points, respectively. Finally, observations based on EGRET [51] and recently on *Fermi* [52] have estimated the cosmic background in gamma-rays from $40\ \mathrm{MeV}$ to 100 GeV. These estimates are shown with dark blue and purple symbols, respectively.

The observational data we have described above give a measurement of the total extragalactic X-ray and gamma-ray background radiation. Over the full energy range, most of the signal is expected to come from photons produced by different astrophysical sources in mechanisms that are unrelated to dark matter annihilation. The contribution from the latter is likely to be a subdominant component of the total signal, which is especially true at lower energies. Upper limits to the emission that have not been accounted for by known sources for $E_0 < 8$ keV, have been found using CHANDRA data (red arrows) [33]. Approximately less than 10% of the integrated specific intensity is unresolved between 1 keV$< E_0 < 8$ keV. For hard X-rays ($10\ \mathrm{keV} \leq E_0 \leq 200\ \mathrm{keV}$), most of the emission is expected to come from Compton-thin Active Galactic Nuclei (AGN). We use the model presented in [48] to put a conservative upper limit on the unresolved component of the emission at these energies (yellow arrows)[82]. The modeling in the MeV range is more uncertain. According to some analyses, blazars are thought to contribute significantly to the radiation [54], but others argue for non-blazar AGNs as the main contributors to the MeV radiation [55]. We will not attempt to model the contribution of these sources due to this controversy, but we note that the constraints on the contribution of dark matter annihilation to the MeV background are expected to be significantly lower than those seen in Fig. 2. Recently, the *Fermi-LAT* collaboration has estimated the blazar contribution to the gamma-ray background in the $0.1 - 100$ GeV energy range. Its total specific intensity in this energy range (i.e. its integrated flux between these energies) down to the minimum detected source flux is $\sim 16\%$ of the derived value for the cosmic gamma-ray background [34]. We use the energy spectrum given by these authors (see their Table 6 and Fig. 20) to account for the blazar contribution noting that this is a conservative estimate since undetected sources certainly contribute to the signal, see below. Star forming galaxies are also expected to be a significant source of gamma-rays in this energy range. We use the model by [35] to include this contribution (see their Fig. 1), which accounts for $\sim 53\%$ of the total specific intensity. We note that the energy spectrum of the contribution of star forming galaxies to the cosmic gamma-ray background (as plotted in Fig. 2, i.e. $E_0 I$) peaks at $E_0 \sim 0.3$ GeV, dominating over the blazar spectrum, and drops more steeply towards higher energies than

the total background. At $E_0 \gtrsim 10$ GeV blazars dominate over star forming galaxies with a spectrum shallower than the observed background. In this way, both populations combined account for $\sim 86\%$ ($\sim 46\%$) of the measured specific intensity at $E_0 \sim 0.3$ GeV ($E_0 \sim 70$ GeV). Over the whole $0.1 - 100$ GeV energy range, they account for $\sim 69\%$ of the total integrated flux. Based on this, the corresponding upper limits on the contribution from additional sources are shown with violet arrows in Fig. 2.

We should comment on the uncertainties associated to the contribution of blazars and star forming galaxies. For the latter, these are connected to the gamma-ray luminosity function of galaxies which is ultimately related to the time-dependent global star formation rate density. The possible behaviors of the gamma-ray luminosity function and the most relevant sources of uncertainty in the model (more importantly the cosmic star formation rate and the normalization given by the inferred gamma-ray luminosity of the Milky-Way) have been considered by [56] using a similar modeling to that of [35]. The authors find that star forming galaxies account for between 10% to 90% of the EBL measured by FERMI at $E_0 \sim 0.3$ GeV (see Fig. 1 of [56]) with a spectral shape very similar to the model we have chosen here. Since the contribution from star forming galaxies is quite uncertain and since the fiducial model we use lies closer to the upper value of this contribution, we explore below the effects that a lower contribution has in our results (see section IV C). If the observed count distribution of blazars is extrapolated to zero flux then their contribution to the total observed signal between 0.1 GeV and 100 GeV is $\sim 23(\pm 9)\%$ (including statistical and systematic uncertainties) [34]. As we mentioned before, this percentage drops to $\sim 16(\pm 9)\%$ when only sources down to the minimum flux are considered. At $E_0 \sim 0.3$ GeV the minimum contribution from blazars to the measured specific intensity is $\sim 7\%$ (including uncertainties). Taking the lower limits of all these uncertainties into account, star forming galaxies and blazars would contribute minimally by $\sim 17\%$ at $E_0 \sim 0.3$ GeV, a factor of 5 lower than the estimate we use here.

B. Constraints on particle physics models

With the procedure we have previously outlined, we can compare the prediction of any given particle physics model with the observational upper limits shown in Fig. 2. The model gives a photon and a positron (electron) input spectra from the annihilation, and our map-making code produces a simulated map for a prescribed energy. A full spectrum can be then produced once maps at different energies are constructed.

It is possible however to present robust limits on the part of the signal that only depends on the intrinsic properties of WIMPs, namely $f_{\rm WIMP}$ in Eq. (1). This can be done by noting that there exists a redshift z^* along the line-of-sight for which Eq. (2) can be written as:

$$I(E_0) = \frac{c}{8\pi} E_0 f_{\rm WIMP}(E_0(1+z^*)) \int \frac{\rho_\chi^2(\vec{x},z) S(\sigma_{\rm vel}(\vec{x},z))}{(1+z)^3} \frac{e^{-\tau(E_0,z)}}{H(z)} {\rm d}z, \quad (12)$$

where $H(z)$ is the Hubble parameter [83]. In general, we do not know the value of z^*, it is model dependent. Nevertheless, we can safely approximate the upper limit of the integral in Eq. (12) by $z = 4$ in the case of the lowest X-ray energies and by $z = 1$ for the higher gamma-ray energies (and values in between for intermediate energies). This is because $\sim 90\%$ of the signal is produced for $z < 4$ ($z < 1$) in the former (latter) case. The relevant redshift range is significantly smaller at higher energies where photon absorption plays an important role. This approximation is good enough for any model with a photon yield spectrum ${\rm d}N/{\rm d}E$ similar to the one depicted in Fig. 1. More generally, for any model with a photon yield that is monotonically decreasing with energy, the large majority of the signal at any given energy would come from relatively low redshifts, since the contribution from higher redshifts would correspond to higher-energy (and hence less abundant) initial photons. This is true because the astrophyisical part of the specific intensity that goes in the integrand of Eq. (12), excluding the absorption factor, is essentially flat with redshift (see for example Fig. 1 of [52]). Thus, we can use the observed upper limits on the unaccounted contribution to $I(E_0)$, and the values of this same quantity predicted by a reference particle physics model to estimate upper limits on $f_{\rm WIMP}(E_0(1+z^*))$:

$$f_{\rm WIMP}(E_0(1+z^*)) \leq f^{\rm REF}_{\rm WIMP}(E_0(1+z^{\rm REF})) \frac{I^{\rm OBS}(E_0)}{I^{\rm REF}(E_0)}, \quad (13)$$

where the values associated with the reference model are given with a superscript REF. The values of z^* and $z^{\rm REF}$ are in the interval $(0,4)$ for $E_0 \sim 10^{-5}$ GeV and in the interval $(0,1)$ for $E_0 \sim 10$ GeV. By choosing $z_{\rm REF} = 0$, so $f^{\rm REF}_{\rm WIMP}$ is evaluated at the measured energy rather than the (higher) effective energy of injection, we obtain a conservative constraint, since this function is monotonically decreasing with respect to energy. Taking a higher value for $z_{\rm REF}$ will strengthen the bound. By choosing $z^* = 0$, we evaluate $f_{\rm WIMP}$ at the lowest possible energy for the purpose of comparing to the limit: this is not conservative for models where $f_{\rm WIMP}$ is a monotonically falling function of energy, in the sense that taking a larger z^* leads to a weaker limit, but since the signal is dominated by the lowest redshifts, the resulting uncertainty is quite small. We denote the upper bound on $f_{\rm WIMP}(E)$ obtained by setting $z^* = z_{\rm REF} = 0$ by $f^{\rm MAX}_{\rm WIMP}(E)$.

We take as a reference model the example we have used throughout the text, and compute $f^{\rm MAX}_{\rm WIMP}$ for the cases without enhancement, and with Sommerfeld boost, off-resonance and near-resonance. The exclusion regions we obtain are shown in Fig. 3 with the light-gray, medium-gray and dark-gray regions, respectively, for these three cases, assuming a minimum extrapolation for the contribution of unresolved substructures to the simulated maps. The dashed lines show how

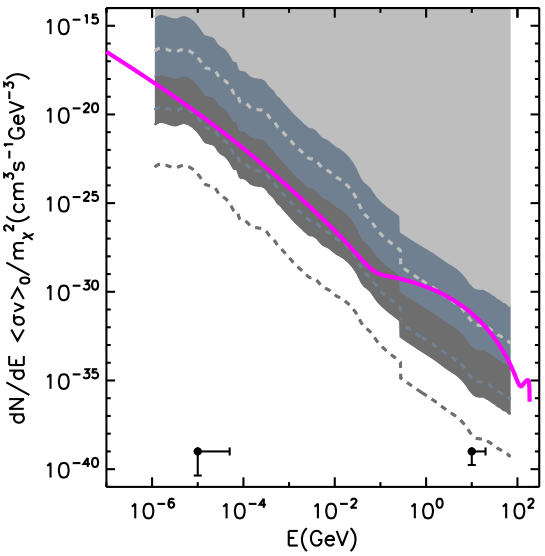

FIG. 3: Limits on the value of $f_{\rm WIMP}$ for dark matter annihilation according to observations of the cosmic X-ray and gamma-ray background radiation. The light-gray, medium-gray and dark-gray areas mark exclusion regions for the case with no Sommerfeld enhancement, off- and near-resonance enhancement, respectively, in the case where the contribution of unresolved substructures to the signal is minimal. The dashed lines show how these regions are extended if this contribution is maximal. The area between the limit of each shaded region and its corresponding dashed line encompasses the uncertainty on the contribution of unresolved subhalos. The symbols with error bars in the bottom show the theoretical uncertainty on the construction of this figure from Fig. 2; see text for details. The thick magenta line is for the SUSY model we have used as an example: a $\sim$ 185 GeV neutralino annihilating into $b\bar{b}$ with $\langle\sigma v\rangle_0 = 6\times10^{-27}{\rm cm}^3{\rm s}^{-1}$.

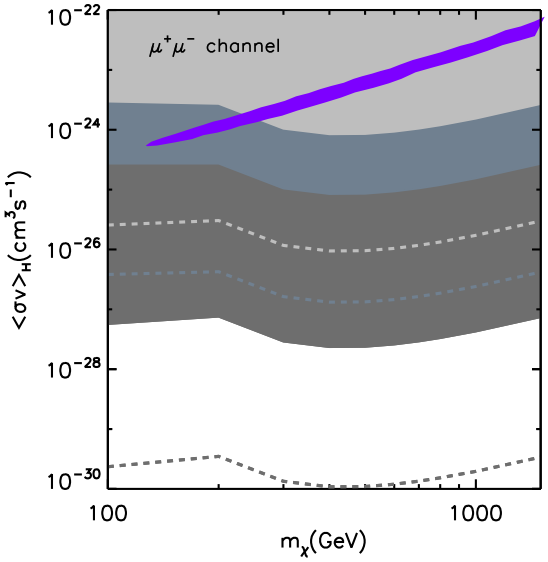

FIG. 4: Constraints on the local value of the thermally averaged annihilation cross section (assuming a MB velocity distribution with $\sigma_{\rm vel} = 150\,{\rm km\,s}^{-1}$) as a function of WIMP mass for annihilation into $\mu^+\mu^-$ final states. These constraints come from observations of the cosmic X-ray and gamma-ray background radiation. The violet contour shows the 2σ best fit region of this model to the PAMELA positron data as presented in [52]. The other line styles and colors are as in Fig. 3.

these exclusion limits are extended if a maximum extrapolation is taken. The right- and down-wards error bars in the figure mark the uncertainty in the values of z^* and $z^{\rm REF}$, respectively. As mentioned before, the amplitude of the uncertainty depends on the value of the observed energy, being lower for higher energies. The thick magenta line shows the value of $f_{\rm WIMP}$ for our reference case.

The validity of a given model can be tested directly using Fig. 3 without the need of computing the CDMAB for this model. Keep in mind that for the cases with Sommerfeld enhancement, the value of $\langle\sigma v\rangle_0$ in $f_{\rm WIMP}$ is the value of the s-wave annihilation cross section without Sommerfeld enhancement.

Once a specific model is chosen, ${\rm d}N/{\rm d}E$ is calculated and Fig. 3 can be used to produce constraints on $\langle\sigma v\rangle_0$ as a function of WIMP mass. As an example, we take a model with annihilation into leptons, specifically $\mu^+\mu^-$ with a branching ratio of 100%. Models such as this are typically used in the literature to explain the anomalous abundance of positrons in cosmic rays above 10 GeV reported by the PAMELA satellite [6]. We use DarkSUSY [43] to compute the in situ positron (electron) and photon spectra. The resulting total photon yield has a very similar shape to the black dotted line shown in Fig. 1, which is by the way shared by all the benchmark models we describe in section IV C. For this case, and for $m_\chi > 100$ GeV, the up-scattered photons contribute dominantly to the background radiation. Instead of showing constraints on $\langle\sigma v\rangle_0$ we show in Fig. 4 the constraints on $\langle\sigma v\rangle_{\rm H} = S(\sigma_{\rm vel} = 150{\rm km s}^{-1})\langle\sigma v\rangle_0$, which is a thermal average over a Maxwell-Boltzmann (MB) velocity distribution with a velocity dispersion of $150\ {\rm km\,s}^{-1}(5\times10^{-4}\ c)$. This roughly corresponds to the estimated local dark matter one-dimensional velocity dispersion. For both cases of Sommerfeld enhancement we are considering: $S(\sigma_{\rm vel} = 150\,{\rm km\,s}^{-1}) \sim 230$. With this choice, we can compare the constraints coming from the extragalactic background radiation with the local values of $\langle\sigma v\rangle$ that better fit the PAMELA data for an explanation of the positron excess based solely on dark matter annihilation. The violet contour in Fig. 4 shows the 2σ best fit region according to [52]. For this particular model with annihilation into $\mu^+\mu^-$ with a branching ratio of 100%, the constraints we find do not favor an explanation of the PAMELA data based only on dark matter annihilation for $m_\chi > 260$ GeV (a similar conclusion was found in [29, 52]). A large saturated Sommerfeld enhancement ($S_{\rm max} > 2000$) essentially rules out this possibility.

We note that any model tested using Fig. 3 also needs to be checked for consistency with the correct relic density. Contrary to Fig. 2 that was used to exemplify a case where a specific model gives the correct dark matter abundance with

and without enhancement (recall that for the former we multiplied the value of $\langle\sigma v\rangle$ without enhancement by a factor f_Ω to accomplish this, see end of section III), the upper limit on $f_{\rm WIMP}$ in Eq. (13) deliberately does not take this into account. In this way, the upper limits on the cases with and without Sommerfeld enhancement in Figs. 3-4 are not related to each other through their values of $\langle\sigma v\rangle_0$.

C. Benchmark models fitting the cosmic ray excesses

In addition to the reference $\mu^+\mu^-$ model, we investigate benchmark models recently presented in [19], which produce the correct thermal relic density, fit the cosmic ray (CR) excesses measured by PAMELA and *Fermi*, and are currently allowed by bounds on $S_{\rm max}$ from the cosmic microwave background. Whereas our previous reference models demonstrate the effect of Sommerfeld enhancement on the EBL constraints in a broad class of scenarios, these benchmarks allow us to test specific proposed models, and compare our bounds to those from the cosmic microwave background. The parameters characterizing these models are summarized in Table I; see [19] for further details [84].

The benchmarks feature dark matter masses in the 1-1.7 TeV range, with nearly-degenerate excited states $\delta \sim 0.1 - 1$ MeV above the ground state. Both Sommerfeld enhancement and annihilation to Standard Model final states occur via vector mediators with masses m_ϕ ranging from $200 - 900$ MeV. These models were chosen to fit the CR data with *no* contribution from local substructure, so they are not perfectly consistent with the assumptions of this work. However, the Sommerfeld enhancement in these models saturates at relatively high velocities in order to evade constraints from the CMB, and thus we expect the substructure boost to the locally measured CR signals to be only a factor of $\sim 1.5 - 5$, based on the results of [57]. We neglect this effect in the following discussion; if the local substructure boost is substantial then these benchmarks would also significantly overpredict e^+e^- cosmic rays, and are less interesting for direct comparisons to data.

Since these benchmark models have lower values of $S_{\rm max}$ than the off-resonance case we considered in Fig. 3, we simply scale-down the upper limits of the latter to the appropriate value of each benchmark model. We note that although $S(\sigma_{\rm vel})$ does not have the same shape for the benchmark models than for the Yukawa case, the previous approximation is good enough because most of the signal comes from structures that are already in the saturated regime. In any case, this approximation actually underestimates the signal from the benchmark models because $S(\sigma_{\rm vel})$ is larger in the intermediate velocity dispersions than in the Yukawa case for the same value of $S_{\rm max}$.

We find that these benchmarks are in conflict with *Fermi* measurements in the energy range $\sim 0.3 - 20$ GeV, even in the case of *minimal* contribution from unresolved substructure, if the current best estimates of contributions from blazars and star-forming galaxies to the EBL are subtracted from the data. The conflict is maximal at $E \sim 300$ MeV, where it is a factor of $\sim 7 - 10$. Fig. 5 displays the ratio $f^{\rm OBS}_{\rm WIMP}/f^{\rm MOD}_{\rm WIMP}$ for these models. With a larger contribution from unresolved substructure, all the benchmarks can be ruled out independent of astrophysical contributions to the EBL.

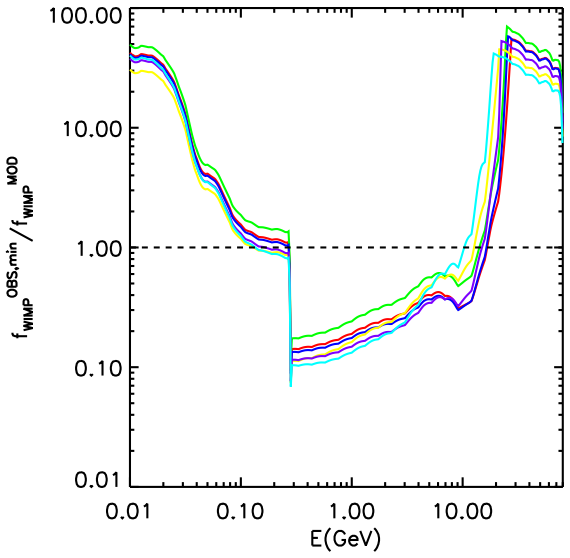

FIG. 5: Ratio of the observed bound on $f_{\rm WIMP}$ to the value predicted by the model, for each of the six benchmarks in Table I: 1=red, 2=green, 3=blue, 4=yellow, 5=violet, 6=cyan. Energies where the ratio is less than 1 are ruled out. For the purposes of this figure, we assume minimal contribution from unresolved substructure.

There are several effects that could ameliorate this conflict, in addition to the small substructure correction mentioned already. The uncertainty on the estimation of $f_{\rm WIMP}$, as shown in Fig. 3, can alleviate the tension slightly (by less than a factor of 2); a potentially larger effect is the uncertainty in the subtraction of astrophysical contributions to the EBL. If our best estimate for the contribution of astrophysical sources is too high (by a factor of up to $\sim$ 5, as discussed previously), then in the case of minimal contribution from unresolved (sub)halos the tension diminishes significantly. In this case however, dark matter annihilation would need to be dominantly responsible for the EBL in the energy range observed by *Fermi*, unless other effects reduce the dark matter signal.

Star forming galaxies dominate the astrophysical gamma-ray background model we have used for $0.3\,{\rm GeV} \lesssim E_0 \lesssim 10\,{\rm GeV}$, whereas blazars dominate at higher energies. The contribution of the former to the total observed signal is particularly important to constrain the role of dark matter annihilation. To illustrate this, we translate the constraints on $f_{\rm WIMP}$ given in Fig. 3 to constraints on the value of the annihilation cross section at saturation by taking the value of $\langle\sigma v\rangle_{\rm sat} = S_{\rm max}\langle\sigma v\rangle_0$ as a free parameter limited by the *Fermi* measurements and the astrophysical background. Fig. 6 shows these constraints as a function of $f^{\rm Fermi}_{\rm SF}(E > 0.1{\rm GeV})$, the contribution of star forming galaxies to the observed integrated flux between 0.1 GeV and 100 GeV. We show the constraints only for the case of minimal contribution of unresolved subhalos.

Benchmark no.	Annihilation Channel	m_ϕ (MeV)	m_χ (TeV)	α_c	δ (MeV)	$\frac{S_{\rm max}\langle\sigma v\rangle_0}{3\times10^{-26}{\rm cm}^3\ {\rm s}^{-1}}$
1	1:1:2 $e^\pm : \mu^\pm : \pi^\pm$	900	1.68	0.04067	0.15	530
2	1:1:2 $e^\pm : \mu^\pm : \pi^\pm$	900	1.52	0.03725	1.34	360
3	1:1:1 $e^\pm : \mu^\pm : \pi^\pm$	580	1.55	0.03523	1.49	437
4	1:1:1 $e^\pm : \mu^\pm : \pi^\pm$	580	1.20	0.03054	1.00	374
5	1:1 $e^\pm : \mu^\pm$	350	1.33	0.02643	1.10	339
6	$e^\pm$ only	200	1.00	0.01622	0.70	171

TABLE I: Particle physics parameters and saturated annihilation cross sections for benchmark points.

The six benchmark models appear with the same colors as in Fig. 5. As a reference, the values of $\langle\sigma v\rangle_{\rm sat}$ that fit the cosmic ray excesses for these models are marked with arrows next to the vertical axis on the right side. The other two models we have used throughout the paper are also included in the figure: $m_\chi = 185$ GeV annihilating into $b\bar{b}$ (magenta line) and $m_\chi = 1.5$ TeV annihilating into $\mu^+\mu^-$ (black line). For the benchmark models and for the $\mu^+\mu^-$ model, the constraint on $\langle\sigma v\rangle_{\rm sat}$ decreases rapidly with $f_{\rm SF}^{\rm Fermi}(E > 0.1{\rm GeV})$, because these models are constrained at $E_0 \sim 0.3$ GeV where the contribution from star forming galaxies peaks. Even assuming only a 5% contribution of star forming galaxies (recall that we have used 53% as a fiducial value), the constraints on $\langle\sigma v\rangle_{\rm sat}$ still exclude the values needed by these models to fit the cosmic ray excesses. The $b\bar{b}$ model is more independent of the star forming contribution since this model is constrained at $E_0 \sim 10$ GeV, where blazars dominate.

We would like to mention that the model we have used to include the contribution from star forming galaxies assumes that the Milky-Way gamma-ray specific intensity has a power law energy spectrum with an exponent of -2.7 for $E \geq 0.6$ GeV [35], which seems to be too steep at high energies according to the recent analysis of the *Fermi-LAT* collaboration that points to an exponent close to -2.5 for $E \geq 10$ GeV (see Table I and Fig. 3 of [58]). Assuming a shallower spectrum for the Milky-Way gamma-ray specific intensity would result in a contribution of star forming galaxies to the EBL with a shallower spectrum as well, making it more relevant at higher energies that it is in the model we have used in this work, and slightly strengthening the derived constraints in Figs. 2,3 and 5 at high energies. Nevertheless, the most relevant uncertainty is the overall contribution of star forming galaxies discussed in the previous paragraph and whose effects are shown in Fig. 6.

We have assumed a low-mass cutoff of $10^{-6}\ M_\odot$: kinetic decoupling can occur quite late in models of this type [59], leading to a higher cutoff of up to $0.1 - 1\ M_\odot$ [60]. However, we estimate that a change of five orders of magnitude in the low-mass cutoff will affect the final result by a factor of only $2 - 6$, and the high end of this range will only be attained for non-minimal contributions from unresolved (sub)halos (i.e., scenarios that are presently in conflict with even the unsubstracted data, for these benchmark models). If the slope we have assumed for the central density profile of the halos is steeper than reality, this could also affect our limits by a factor of a few: the NFW profile we have chosen lies between the Moore and Burkert profiles considered by [29], and the difference between those profiles modifies the gamma-ray signal by roughly an order of magnitude. The presence of significant dark matter self-interactions and nearly-degenerate excited states in models of this type can lead to disruption of low-mass halos and the depletion of central density cusps (see e.g. [61, 62] and references therein); while these effects could potentially reduce the tension with the EBL data, their inclusion is beyond the scope of our current analysis.

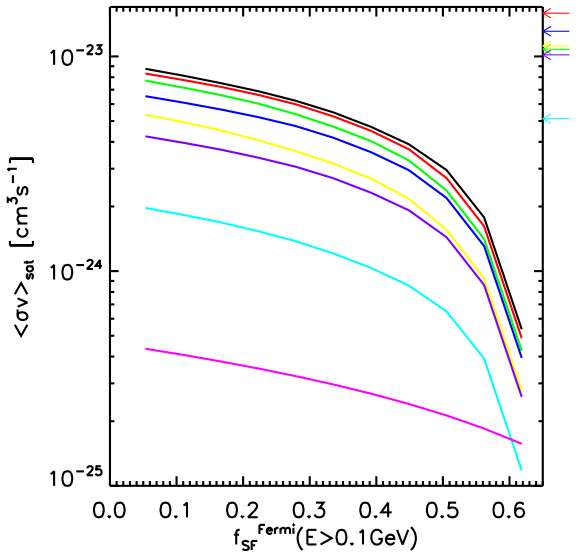

FIG. 6: Constraints to the annihilation cross section at saturation as a function of the contribution from star forming galaxies to the observed integrated flux between 0.1 GeV and 100 GeV as measured by *Fermi*. The values above the lines are excluded. We have taken the model given in [35] to get the spectral shape of this contribution. We show the six benchmark models of Table 1, setting $\langle\sigma v\rangle_{\rm sat}$ as a free parameter, with the same colors as in Fig. 5. The small arrows next to the vertical axis on the right side mark the corresponding values of $\langle\sigma v\rangle_{\rm sat}$ for these benchmarks as given in Table 1. We also show the results for a model with annihilation into $\mu^+\mu^-$ and a mass of 1.5 TeV (black line), and the model we used as reference in Figs. 1-3: a 185 GeV neutralino annihilating into $b\bar{b}$ (magenta line). As in Fig. 5 we have assumed a minimal contribution from unresolved substructures. Blazars are assumed to contribute by a fixed amount (16%) in the energy range measured by *Fermi* [34].

We therefore see that in a CDM scenario, in the context of current structure formation models, the EBL can robustly act

as a more sensitive probe of Sommerfeld-enhanced dark matter annihilation scenarios than the cosmic microwave background. Removing tension with the EBL for the benchmark models we have tested seems to demand minimal contributions to the signal from unresolved substructure, and *in addition* either dark matter structure formation must be modified from a pure collisionless CDM scenario, or the contribution to the EBL from blazars and galaxies must be at the low end of current estimates.

V. SUMMARY AND CONCLUSIONS

A positive detection of a non-gravitational signature of dark matter would be a breakthrough in our understanding of this still mysterious form of matter. Current experiments on Earth looking for signals of interactions between dark and ordinary matter intensify the efforts to reach the necessary sensitivities to either largely constrain the parameter space of minimal SUSY theories that predict the favorite dark matter candidate, the neutralino, or to find a definite signal [63].

The existence of dark matter could also be confirmed through the detection of ordinary matter produced during the annihilation of WIMPs in regions of high dark matter density. This annihilation is expected to produce a population of gamma-ray photons that would make dark matter halos visible in the gamma-ray sky. The cumulative effect of these gamma-rays produced outside our galactic halo creates a cosmic background that adds up to the one produced by other sources such as blazars and star forming galaxies.

This hypothetical background radiation is also populated at lower energies by a fraction of the original CMB photons that on their journey towards us are scattered by energetic electrons and positrons produced during the annihilation of WIMPs. They gain energy in the process and reach us as X-ray and gamma-ray photons.

In this work, we have used the state-of-the-art Millennium II simulation [37] that follows the formation and evolution of structure formation in a ΛCDM cosmology, to produce simulated sky maps of this conjectured cosmic background. Our method includes the signal coming from all halos and subhalos resolved in the simulation as well as a careful extrapolation to account for the contribution of unresolved structures that are expected to exist all the way down to masses of about ~ 1 Earth mass, that correspond to the damping mass limit of one of the most studied type of WIMPs: ~ 100 GeV neutralino.

This paper extends the analysis of [36] by including: i) the X-ray and soft gamma-ray contribution to the background radiation by CMB photons that gain energy through Inverse Compton scattering of the electrons and positrons produced during annihilation [85]; ii) a detailed treatment of a Sommerfeld mechanism that enhances the annihilation cross section, leading to a significantly larger annihilation rate from dark matter structures with low velocity dispersions. The Sommerfeld enhancement has been invoked to explain the anomalous excess of cosmic ray positrons above 10 GeV reported by the PAMELA satellite (e.g. [11]). We present results using this enhancement for two sets of parameters chosen to represent typical cases: i) an off-resonance case where the boost to the annihilation cross section scales as $1/\sigma_{\rm vel}$, and ii) a near-resonance case where the boost goes as $1/\sigma^2_{\rm vel}$.

We have found that observational upper limits on the unknown contributions to the X-ray and gamma-ray background radiation put significant constraints on the contribution from dark matter annihilation (see Fig. 2 for a comparison with a particular model). These upper limits are especially stringent in the gamma-ray regime due to recent measurements reported by the *Fermi-LAT* experiment, together with well-founded expectations for the contributions of blazars and star-forming galaxies [34, 35, 52].

We introduced a model-independent way to give constraints on the intrinsic properties of WIMPs by "factoring-out" the astrophysical part of the signal, namely, the one that depends on the density field of dark matter, which is accurately given by the N-body simulation we have used. The constraints we obtain for the remaining "particle physics" factor ($f_{\rm WIMP}$, see Eq. 1), appear on Fig. 3. This figure can be used as a template to test whether or not a given particle physics model violates the observational constraints. Although for the case with Sommerfeld enhancement we only presented two particular cases, Fig. 3 can still be easily used to scale the constraints up or down for other realizations of these types of models.

By selecting a particle physics model and computing the photon yield $\mathrm{d}N/\mathrm{d}E$ (composed by in situ and up-scattered CMB photons, see sections II A, II B and Fig. 1), it is possible to give direct constraints for the annihilation cross section as a function of WIMP mass. We show an example of this in Fig. 4, where a model annihilating into $\mu^+\mu^-$ final states was chosen. For this particular model, the constraints we obtain disfavor the scenario where the positron excess measured by the PAMELA satellite is explained by dark matter annihilation alone (of course, there could still be some subdominant DM contribution to the signal). Furthermore, we have presented constraints on specific "benchmark" Sommerfeld-enhanced models selected to fit the cosmic ray spectra measured by PAMELA and *Fermi* without any contribution from local substructure, while obtaining the correct relic density and respecting bounds from the cosmic microwave background. We find that these models are in conflict with our constraints, even in the case of minimal contributions from unresolved substructure. This tension could diminish significantly if the contribution to the cosmic gamma-ray background from blazars and star forming galaxies is quite low (current uncertainties are still large, particularly in the latter, and put a minimum value of 17% of the observed signal at $E \sim 0.3$ GeV which is a factor of 5 lower than the estimate we have used here, see the last paragraph of section IV A). Another interesting possibility to reconcile these models lies in taking into account the role of self-interactions between dark matter particles, inherent in the models, in the formation and evolution of dark matter structures (this can lead for example to the formation of central density cores in low-mass halos [61]).

The main sources of uncertainty in our modelling from the astrophysical part of the signal are, in order of importance: i) the contribution of unresolved substructures, which is uncertain by roughly two orders of magnitude; ii) the concentration

of dark matter in the inner part of halos. In this work we have used a NFW density profile. If an Einasto profile is used instead, which is currently favored by high resolution simulations of single halos, the annihilation rate for each halo is increased by 50% [36]; iii) the value of the minimum mass of bound halos made of WIMPs; iv) the approximations used for electron and positron losses, and photon absorption (see Appendices A and B).

It is worth mentioning that the fine-grained structure of dark matter halos is predicted to be a superposition of streams with very small internal velocity dispersions. If the annihilation cross section is independent of the velocity dispersion, then the contribution of these fundamental streams and their associated caustics to the annihilation rate is essentially negligible [9]. However, this could change dramatically in Sommerfeld-enhanced models due to the large boosts expected in the streams. We explore this in appendix D and find that despite the more prominent role of streams in these type of models, their contribution is still significantly smaller than that of subhalos, due to the saturation of the enhancement at low velocities, and can be safely neglected.

In spite of these uncertainties, and thanks to increasingly better measurements of the cosmic X-ray and gamma-ray background radiation, and to our better understanding of the contribution to it by AGNs, blazars and star-forming galaxies, an analysis like ours produces competitive constraints compared to those obtained in other indirect searches, such as those based on dwarf galaxies [64]. Our work can also be viewed as complementing that of other works [29–31], that have presented a similar analysis using analytical approaches to model the astrophysical part of the signal instead of high resolution N-body simulation, as we have done here.

Acknowledgments

We would like to thank Neal Weiner, Simon D. M. White, Niayesh Afshordi and Mattia Fornasa for interesting comments and suggestions. JZ acknowledges financial support by the Joint Postdoctoral Program in Astrophysical Cosmology of the Max Planck Institute for Astrophysics and the Shanghai Astronomical Observatory, and from a CITA National Fellowship. This work was supported in part by NSF grant AST-0907890 and NASA grants NNX08AL43G and NNA09DB30A (for A.L.). TS gratefully acknowledges support from the Institute for Advanced Study. The research of TS is supported by the DOE under grant DE-FG02-90ER40542 and the NSF under grant AST-0807444.

Appendix A: Energy losses for electrons and positrons

The processes briefly summarized here are described in detail in [65]. Since the CMB energy density scales with redshift as $(1+z)^4$, the energy loss term due to IC scattering with the CMB photons is given by:

$$b_{\rm e}(E_{\rm e},z)_{\rm ic} \approx 2.5\times10^{-17}(1+z)^4\left(\frac{E_{\rm e}}{\rm GeV}\right)^2 \ {\rm GeV/s} \quad \text{(A1)}$$

The energy loss due to synchrotron radiation in the ambient magnetic field B, which has a spatial and temporal functional dependence, is given by:

$$b_{\rm e}(E_{\rm e},z)_{\rm syn} \approx 0.254\times10^{-17}\left(\frac{B}{1\mu{\rm G}}\right)^2\left(\frac{E_{\rm e}}{\rm GeV}\right)^2 \ {\rm GeV/s} \quad \text{(A2)}$$

The magnitude of the magnetic field has large spatial variations, going from $\sim 10\mu$G in the cores of galaxy clusters [66] to $\sim 0.1\mu$G in the intergalactic medium in clusters [67]. Thus, synchrotron losses are expected to be comparable to IC losses only in the regions with the strongest magnetic fields, such as the centers of galaxy clusters. Although dark matter annihilation is copious in high density regions such as these, the contribution from subhalos and low-mass halos is in average more significant than the one from the center of massive halos associated to galaxy clusters. Furthermore, the strength of the magnetic field is not expected to increase as rapidly with redshift as the CMB energy density. This makes the synchrotron losses less significant than the IC losses at high redshifts.

The electrons and positrons produced in the annihilation process also lose energy due to ionisation of neutral atoms and Coulomb scattering with free electrons present in the ambient field. The energy loss rate of both processes is essentially independent of energy and is given by:

$$b_{\rm e}(E_{\rm e},z)_{\rm ion} \approx 18.4\times10^{-17}\left(\frac{n_{\rm H}}{\rm cm^{-3}}\right) \ {\rm GeV/s} \quad \text{(A3)}$$

$$b_{\rm e}(E_{\rm e},z)_{\rm coul} \approx 55.4\times10^{-17}\left(\frac{n_{\rm e}}{\rm cm^{-3}}\right) \ {\rm GeV/s} \quad \text{(A4)}$$

where $n_{\rm H}$ and $n_{\rm e}$ are the local number densities of neutral hydrogen and free electrons, respectively. Bremsstrahlung radiation is another source of energy loss that also depends on the local density of the ambient ionized and neutral material. In the weak-shielding limit the energy loss rate due to Bremsstrahlung is given by:

$$b_{\rm e}(E_{\rm e},z)_{\rm brem} \approx 15.1\times10^{-17}\left(\frac{E_{\rm e}}{\rm GeV}\right)\left(\frac{n_{\rm e}}{\rm cm^{-3}}\right) \ {\rm GeV/s} \quad \text{(A5)}$$

At high electron energies, the latter three processes are subdominant relative to the IC losses due to the energy squared dependence in Eq. (A1). At low energies they become more significant but are nevertheless suppressed by the average low density of the ambient medium. This can be seen by noting that the minimum energies we are interested in are those corresponding to the soft X-rays ($E_{\rm IC} \gtrsim 10^{-7}$GeV) coming from the IC scatter of CMB photons. An up-scattered CMB photon will have an average energy of: $E_{\rm IC} \approx 4/3(E_{\rm e}/m_{\rm e})^2E$ [68], where $E_{\rm e}$ and $m_{\rm e}$ are the energy and mass of the scattering electron, and E is the energy of the photon before the event, thus for $E_{\rm IC}\sim10^{-7}$ GeV the electron energies of relevance are of the order of 0.25 GeV at $z=0$. For these energies, ionisation, coulomb and bremsstrahlung losses dominate over IC losses only if the ambient density of electrons

and neutral hydrogen is $\gtrsim 10^{-2}$ cm^{-3}. In the local ISM $n_{\rm e} \sim 0.1$ cm^{-3} [69]. In galaxy clusters the average gas density is $\sim 10^{-3}$ cm^{-3} [38] and in dwarf spheroidals like Draco it is $\sim 10^{-6}$ cm^{-3} [70]. Since the largest contribution to the production of electrons and positrons comes from the accumulated effect of annihilation in low-mass halos and subhalos, which have clearly low ambient densities of ordinary matter, we can safely neglect the impact of these three processes of energy loss. They could be of relevance in the center of massive halos at low redshift, but they are negligible for the overall full-sky signal.

Appendix B: Photon absorption

For energies $\gtrsim 10$ GeV measured at $z = 0$, the dominant mechanism of photon absorption is that due to the interaction between the gamma-ray photons produced in the annihilation process and the lower energy starlight photons produced in galaxies (i.e., pair production with the ambient photon field). As mentioned in Section II, this absorption is parameterised as an exponential term with an effective optical depth $\tau(E_0, z)$. We adopt the most recent treatment of [71] to calculate the values of the optical depth as a function of energy and redshift. For this purpose, we take their fiducial 1.2 model and make a bilinear interpolation following their Fig. 11.

For lower observed energies down to $\sim 10^{-6}$ GeV, the Universe is basically transparent to photons produced at any given redshift between $z = 0$ and $z = 10$ (e.g. Fig. 3 of [31]). In this paper we are considering a range of energies that extends slightly towards lower energies (10^{-7} GeV). In this regime, photoionization and Compton scattering are important mechanisms of energy loss. As can be seen from Fig. 3 of [31], $\tau \sim 1$ at these energies for photon sources located at $z \sim 7$. This means that these processes would suppress an important fraction of photons coming from dark matter structures at $z \gtrsim 7$. However, most of the emission from annihilation comes from sources at $z \lesssim 3$ ($\sim 60\%$ of the total emission at these energies), which is a region essentially transparent. Thus, we are ignoring these mechanisms noting that we could be overestimating the predicted signal at the percent level, which is clearly a minor effect for the purposes of this work.

Appendix C: The astrophysical factor, luminosity from halos and subhalos

1. Resolved structures

The total annihilation luminosity (including in situ and upscattered photons) coming from a halo (or subhalo) of volume V is given by:

$$L_{\rm h} = \int_{\rm V} \mathcal{E}(\vec{x})\, {\rm d}V = \frac{E}{2} f_{\rm WIMP} \int_{\rm V} \rho_\chi(\vec{x})^2 S(\sigma_{\rm vel}(\vec{x}))\, {\rm d}V = \frac{E}{2} f_{\rm WIMP} L'_{\rm h}. \quad \text{(C1)}$$

We assume that halos (or subhalos) have a NFW density profile[86] [72], and an average boost factor $S(\bar{\sigma}_{\rm vel})$ given by the mean velocity dispersion of its particles. Thus:

$$L'_{\rm h} = S(\bar{\sigma}_{\rm vel}) \int \rho^2_{\rm NFW}(r)\, {\rm d}V = S(\bar{\sigma}_{\rm vel}) \frac{1.23\, V^4_{\rm max}}{G^2 r_{\rm max}}, \quad \text{(C2)}$$

where the last scaling relation was found by [42] with $r_{\rm max}$ being the radius where the rotation curve reaches its maximum $V_{\rm max}$. It is important to consider the impact of numerical resolution on the values of $r_{\rm max}$ and $V_{\rm max}$. The values of $r_{\rm max}$ are increasingly overestimated for smaller structures whereas the opposite is true for $V_{\rm max}$ [36, 73]. We have hence corrected these quantities following the prescription of [36].

2. Unresolved structures

The previous description is used for all structures that are resolved by the MS-II simulation. However, we want to obtain predictions down to the minimum mass for bound WIMP halos. For neutralinos this is $\lesssim 1 {\rm M}_\oplus$, which clearly lies many orders of magnitude below current simulations. For ~ 100 GeV neutralinos, the damping mass lies in the range $10^{-8} - 10^{-4}$ M$_\odot$, whereas for ~ 1 TeV neutralinos, the range is $10^{-11} - 10^{-7}$ M$_\odot$. For simplicity, we assume that these reference values for neutralinos are generically valid for other WIMPs and choose a fiducial value of $10^{-6} h^{-1} {\rm M}_\odot$ for all the cases we analyze in this paper, noting that the precise value of this mass is a source of uncertainty in our results.

To incorporate these unresolved structures into our maps, we follow an analogous procedure to the one developed in [36], that we briefly describe in the following, dividing it into unresolved main halos and unresolved subhalos.

a. Unresolved halos

The total annihilation luminosity coming from main halos in a given mass range can be computed using the function:

$$F_{\rm h}(M_{\rm h}) = \frac{\sum L'_{\rm h}}{\bar{M}_{\rm h} \Delta \log M_{\rm h}}, \quad \text{(C3)}$$

where the sum is over all the luminosities $L'_{\rm h}$ of halos (given by Eq. C2) with masses in the range: $\log M_{\rm h} \pm \Delta \log M_{\rm h}/2$, and $\bar{M}_{\rm h}$ is the mean halo mass in each bin. In the absence of Sommerfeld enhancement the function $F_{\rm h}(M_{\rm h})$, henceforth called: $F^{\rm NSE}_{\rm h}(M_{\rm h})$, is a power law in the intermediate to low mass regime (see Fig. 4 of [36]). Once the Sommerfeld boost is applied to each main halo, the power law behavior of $F_{\rm h}(M_{\rm h})$ is modified by the function $S(\bar{\sigma}_{\rm vel})$.

The minimum halo mass we can rely on to compute $F_{\rm h}(M_{\rm h})$ is $M_{\rm lim} = 6.89 \times 10^8\, h^{-1} {\rm M}_\odot$ (100 simulation particles). Below this mass we need to extrapolate $F_{\rm h}(M_{\rm h})$ using the information we have on $S(\bar{\sigma}_{\rm vel})$, and on the extrapolation made for $F^{\rm NSE}_{\rm h}(M_{\rm h})$. The value of $M_{\rm lim}$ translates into a limiting value of $\sigma_{\rm vel}$ that we obtain directly from the simulation data: $\sigma_{\rm vel,lim}(z = 0) \sim 3.4 \times 10^{-5}$ [87]. Therefore, we obtain

a fit to the power law behavior of $F_{\rm h}(M_{\rm h})$ in the last resolved mass range of the MS-II and extrapolate this function down to the damping mass limit taking into account the saturation of $S(\bar{\sigma}_{\rm vel})$.

The ratio of annihilation emission coming from all halos contained in a cosmic volume $V_{\rm B}$ with masses larger than $M_{\rm min}$ to the emission produced by a smooth homogeneous distribution of dark matter, with average density $\bar{\rho}_{\rm B}$, filling this volume is approximately given by:

$$f(M_{\rm h} > M_{\rm min}) \sim \frac{1}{\bar{\rho}_{\rm B}^2 V_{\rm B}} \int_{M_{\rm min}}^{\infty} \frac{F_{\rm h}(M_{\rm h})}{\ln 10}\, {\rm d}M_{\rm h}. \qquad \text{(C4)}$$

For a given redshift, the ratio of the values of $f(M_{\rm h} > M_{\rm min})$ with and without enhancement below the saturation mass is roughly given by $S_{\rm max}$.

Using Eq. (C4), we estimate the contribution from the unresolved main halos down to the damping mass limit by assuming that the radiation from the missing halos in the mass range $10^{-6}\ h^{-1}{\rm M}_\odot$ to $\sim 6.89\times10^8\ h^{-1}{\rm M}_\odot$ is distributed on the sky in the same way as the one from the smallest masses we can resolve in the simulation, which we adopt as the mass range between $1.4\times10^8\ h^{-1}{\rm M}_\odot$ and $\sim 6.89\times10^8\ h^{-1}{\rm M}_\odot$ (halos with 20 to 100 particles). This assumption is justified because the clustering bias seems to asymptotically approach a constant value for low halo masses [37].

Using the extrapolated behavior of $F_{\rm h}(M_{\rm h})$ in Eq. (C4) we compute the boost factor $b_{\rm h}$ by which each halo in the mass range $1.4 - 6.89\times10^8\ h^{-1}{\rm M}_\odot$ needs to be multiplied such that the luminosity of the unresolved main halos is accounted for as well:

$$\begin{aligned} b_{\rm h}^{({\rm NSE},i,ii)} &= \frac{f(10^{-6}\ h^{-1}{\rm M}_\odot, 6.89\times10^8\ h^{-1}{\rm M}_\odot)_{\rm a}}{f(1.4\times10^8\ h^{-1}{\rm M}_\odot, 6.89\times10^8\ h^{-1}{\rm M}_\odot)_{\rm sim}} \\ &\sim (60, 90, 2.4\times10^3) \end{aligned} \qquad \text{(C5)}$$

Note that $b_{\rm h}$ is effectively the ratio of $f(M_{\rm h} > M_{\rm min})$ computed analytically between the cutoff mass limit and the 100 particle limit, and computed in the simulation for the lowest resolved mass range. The superscripts (NSE, i, ii) are for the cases without Sommerfeld enhancement, off-resonance ($S_{\rm max} = 2000$) and near-resonance ($S_{\rm max} = 10^6$), respectively. The value of $b_{\rm h}$ is nearly independent of redshift up to $z = 2.1$. For higher redshifts, the power law fit to Eq. (C3) is unreliable for the extrapolation because the population of halos over the resolved mass range becomes too small.

b. *Unresolved subhalos*

Cold dark matter halos contain numerous substructures that contribute significantly to their total annihilation luminosity. For massive halos, this contribution largely exceeds that of the smooth main halo. For a MW-like halo the total luminosity from all its subhalos down to the damping mass is between 2 and 2000 times larger than its own smooth component [36].

The Sommerfeld mechanism increases the contribution of substructures even further due to their low velocity dispersion relative to that of their host. We now calculate the contribution from unresolved subhalos following an analogous procedure to the one described in [36]. It follows a methodology similar to that of the previous subsection and rests on the analysis of the following quantity:

$$F_{\rm sub}\left(\frac{M_{\rm sub}}{M_{\rm h}}\right) = \left(\frac{M_{\rm h}}{L'_{\rm h}}\right) \frac{\sum L'_{\rm sub}}{\bar{M}_{\rm sub}\Delta\log M_{\rm sub}}, \qquad \text{(C6)}$$

where $M_{\rm sub}$ and $L'_{\rm sub}$ (given by Eq. (C2) are the mass and luminosity of a given subhalo. The total luminosity of all subhalos relative to that of their host is given by:

$$f_{\rm sub}(M_{\rm sub}^{\rm max}, M_{\rm h}) \sim \frac{1}{L'_{\rm h}} \int_{10^{-6}}^{M_{\rm sub}^{\rm max}} \left(\frac{L'_{\rm h}}{M_{\rm h}}\right) \frac{F_{\rm sub}\left(\frac{M_{\rm sub}}{M_{\rm h}}\right)}{\ln 10} {\rm d}M_{\rm sub}, \qquad \text{(C7)}$$

where $M_{\rm sub}^{\rm max}$ is the mass of the most massive subhalo within the host.

To simplify the analysis of $F_{\rm sub}$ in the case of Sommerfeld enhancement, we approximate $F_{\rm sub}$ by:

$$F_{\rm sub} \sim \left(\frac{M_{\rm h}}{\bar{S}(M_{\rm h}) L'^{\rm NSE}_{\rm h}}\right) \frac{\bar{S}(M_{\rm sub})\sum L'^{\rm NSE}_{\rm sub}}{\bar{M}_{\rm sub}\Delta\log M_{\rm sub}} = \frac{\bar{S}(M_{\rm sub})}{\bar{S}(M_{\rm h})} F^{\rm NSE}_{\rm sub} \qquad \text{(C8)}$$

where $\bar{S}(M_{\rm h})$ and $\bar{S}(M_{\rm sub})$ are average enhancements for $M_{\rm h}$ and for the subhalo mass range: $\log M_{\rm sub} \pm \Delta\log M_{\rm sub}/2$, respectively. These averages are given by the combination of $\sigma_{\rm vel}(M)$ and $S(\sigma_{\rm vel})$, and we obtain them directly by fitting the simulation data.

The average boost as a function of halo mass and redshift is well described by:

$$(\bar{S}(M_{\rm h}, z))_{(i,ii)} = (S_{\rm h,0} G_{\rm h}(z) M_{\rm h}^{\alpha_{\rm h}^{\rm SE}})_{(i,ii)}, \qquad \text{(C9)}$$

where $S_{\rm h,0}$ is a normalization factor and all redshift dependence has been put into $G_{\rm h}(z)$ (recall that this dependence comes from the $\sigma_{\rm vel}(M_{\rm h})$ relation).

For case i), there are two characteristic masses that mark the transitions below which $S \to S_{\rm max}$ and above which $S \to 1$. The characteristic masses are redshift dependent and can be obtained by matching the three regimes. For case ii), there are three such characteristic masses marking the transition between saturation, $S \sim 1/\sigma^2_{\rm vel}$, $S \sim 1/\sigma_{\rm vel}$ and $S \to 1$. For both cases we find that the fitting functions are a very good approximation up to $z = 2.1$.

For subhalos we apply a similar procedure using:

$$(\bar{S}(M_{\rm sub}, z; M_{\rm h}))_{(i,ii)} = (S_{\rm sub,0} G_{\rm sub}(z) M_{\rm sub}^{\alpha_{\rm sub}^{\rm SE}})_{(i,ii)}, \qquad \text{(C10)}$$

which has the same functional form as Eq. (C9) but with an implicit dependence on the mass of the host which takes care of the fact that subhalos can only have Sommerfeld boosts that are larger than those of their hosts. Thus, if for example a host is saturated, all its subhalos are saturated as well and we have $\bar{S}_{\rm sub} = \bar{S}_{\rm h}$. For this particular case it is easy to see that the contribution of substructures to the luminosity of the halo is the same as in the case without enhancement: $f_{\rm sub} = f^{\rm NSE}_{\rm sub}$. To obtain the parameters in Eq. (C10) we only analyze main halos with more than 500 subhalos.

In both cases the different regimes are divided by transition subhalo masses analogous to the ones for hosts. The fitting procedure is less reliable than in the case of halos. In particular, the scatter on the slope of the power law for a given redshift, measured with quartiles, is of the order of 10%, and the median can change up to the same amount between $z = 0$ and $z = 2.1$. The scatter of the normalization at a given redshift is of the order of a factor of 2, and for different redshifts, its median can change up to a factor of 4.

As for halos, we consider the subhalo population to be complete down to $M_{\rm lim} = 6.89 \times 10^8\, h^{-1}{\rm M}_\odot$. Below this mass, we use Eqs. (C7-C10) to add the contribution of unresolved subhalos to each of the resolved halos. The value of $M_{\rm sub}^{\rm max}$ in Eq. (C7) is given by $M_{\rm sub}^{\rm max} = M_{\rm lim}$ if the halo has subhalos and $M_{\rm sub}^{\rm max} = f_{\rm max} M_{\rm h}$, with $f_{\rm max} = 0.05$ otherwise. In the former case we distribute the missing luminosity among all resolved subhalos, in the latter we simply add it to the host. The precise value of $f_{\rm max}$ has little impact on the results.

Considering resolved an unresolved subhalos we find that a halo of $10^{12}\, h^{-1}{\rm M}_\odot$ has $f_{\rm sub} \in (11, 1.04 \times 10^4)$ for case i), and $f_{\rm sub} \in (4.13 \times 10^3, 6.86 \times 10^6)$ for case ii), that is ~ 6, ~ 3000 times more than in the case without Sommerfeld enhancement, respectively.

Finally, we need to add the subhalo contribution to all main halos with masses below $M_{\rm lim}$. To do so, we compute an overall boost factor $b_{\rm sub}$ to the luminosity of all main halos between the damping scale limit and $M_{\rm lim}$:

$$b_{\rm sub} = \frac{\mathfrak{f}_{\rm boost}(10^{-6}\, h^{-1}{\rm M}_\odot, 6.89 \times 10^8\, h^{-1}{\rm M}_\odot)}{\mathfrak{f}_{\rm no-boost}(10^{-6}\, h^{-1}{\rm M}_\odot, 6.89 \times 10^8\, h^{-1}{\rm M}_\odot)} \tag{C11}$$

where $\mathfrak{f}_{\rm no-boost}$ is given by:

$$\mathfrak{f}_{\rm no-boost}(10^{-6}\, h^{-1}{\rm M}_\odot, 6.89 \times 10^8\, h^{-1}{\rm M}_\odot) \approx \int_{10^{-6}}^{6.89\times10^8} \frac{F_{\rm h}(M_{\rm h})}{\ln 10}\, {\rm d}M_{\rm h} \tag{C12}$$

and $\mathfrak{f}_{\rm boost}$ can be written as:

$$\mathfrak{f}_{\rm boost}(10^{-6}\, h^{-1}{\rm M}_\odot, 6.89 \times 10^8\, h^{-1}{\rm M}_\odot) \approx \int_{10^{-6}}^{6.89\times10^8} [1 + f_{\rm sub}(f_{\rm max} M_{\rm h}, M_{\rm h})] \frac{F_{\rm h}(M_{\rm h})}{\ln 10}\, {\rm d}M_{\rm h}. \tag{C13}$$

For the cases with Sommerfeld enhancement, Eq. (C11) can be simplified by noting the following. The integral in Eq. (C12) is dominated by the mass range where the Sommerfeld enhancement is already saturated, this is because $F_{\rm h}$ is always a power law, monotonically increasing with mass, and the saturation mass ($M_{\rm h,sat}$) is relatively close to $M_{\rm lim}$ and much larger than the damping mass. For instance in case i), $M_{\rm h,sat} \sim 7 \times 10^8\, h^{-1}{\rm M}_\odot (1+z)^{-1}$, thus even at high redshifts, the contribution of the unsaturated part is always negligible. In case ii), $M_{\rm h,sat} \sim 1.5 \times 10^5\, h^{-1}{\rm M}_\odot (1+z)^{-0.8}$, which means that the aforementioned contribution is larger than in case i) but we still find it to contribute minimally to the integral, less than 10%. Therefore, we can approximate Eq. (C12) by: $\mathfrak{f}_{\rm no-boost} \approx S_{\rm max} \mathfrak{f}^{\rm NSE}_{\rm no-boost}$, where $\mathfrak{f}^{\rm NSE}_{\rm no-boost}$ is the value of Eq. (C12) in the case of no Sommerfeld enhancement. For case i), a similar approximation can be used to simplify Eq. (C13). It can be shown that $f_{\rm sub} \approx f^{\rm NSE}_{\rm sub}$ and since $F_{\rm h} \approx S_{\rm max} F^{\rm NSE}_{\rm h}$, then $\mathfrak{f}_{\rm boost} \approx S_{\rm max} \mathfrak{f}^{\rm NSE}_{\rm boost}$. Thus, for case i) we have that:

$${b_{\rm sub}}^{(i)} \approx b^{\rm NSE}_{\rm sub} \in (2, 60) \tag{C14}$$

where the numerical values were obtained for the case of no enhancement in [36].

The case of resonant enhancement is more complex, since the saturation mass is lower than in the non-resonant case and thus the non-saturated regime has a more relevant influence on $\mathfrak{f}_{\rm boost}$. However, we can show that in general:

$$\mathfrak{f}_{\rm boost} \leq S_{\rm max} \mathfrak{f}^{\rm NSE}_{\rm boost}. \tag{C15}$$

To prove this we note that since $\mathfrak{f}_{\rm no-boost} \approx S_{\rm max} \mathfrak{f}^{\rm NSE}_{\rm no-boost}$, thus $\mathfrak{f}_{\rm boost} = \mathfrak{f}_{\rm no-boost} + [...] = S_{\rm max} \mathfrak{f}^{\rm NSE}_{\rm no-boost} + [...]$. Therefore to prove Eq. (C15) we just need to show that:

$$\int_{10^{-6}}^{6.89\times10^8} f_{\rm sub} F_{\rm h}\, {\rm d}M_{\rm h} \leq S_{\rm max} \int_{10^{-6}}^{6.89\times10^8} f^{\rm NSE}_{\rm sub} F^{\rm NSE}_{\rm h}\, {\rm d}M_{\rm h}. \tag{C16}$$

This is true because each subhalo in a host can be enhanced by $S_{\rm max}$ at the most, that means that the total luminosity of all these subhalos is bounded by $S_{\rm max}$: $f_{\rm sub} L'_{\rm h} \leq S_{\rm max} (f_{\rm sub} L'_{\rm h})^{\rm NSE}$. Since by definition $F_{\rm h} \sim \ln(10) L'_{\rm h} {\rm d}N_{\rm h}/{\rm d}M_{\rm h}$, where ${\rm d}N_{\rm h}/{\rm d}M_{\rm h}$ is the number of halos in the mass range $M_{\rm h} \pm {\rm d}M_{\rm h}$, we have that: $f_{\rm sub} F_{\rm h} \leq S_{\rm max} (f_{\rm sub} F_{\rm h})^{\rm NSE}$, which proves Eq. (C16). After doing the calculation we find that:

$${b_{\rm sub}}^{(ii)} \in (2, 42) \tag{C17}$$

We take the range of values in Eqs. (C14-C17) as extrema reflecting the uncertainties on the extrapolation procedure. They should then bracket the true result.

Appendix D: Annihilation in fundamental streams

To compute the luminosity coming from annihilation in streams, we use the methodology described in [8, 9] that integrates the geodesic deviation equation together with the N-body equations of motion to follow the evolution of the fine-grained structure of dark matter halos. This method was applied to the Milky-Way size objects simulated by the Aquarius project in [9], we took their results from one of these objects.

In Fig. 7, we show the spherically averaged radial profiles of the annihilation luminosity for the smooth halo component (red), computed using the local mean density, and for the fine-grained intra-stream component (blue). The solid and dashed lines are for the differential and cumulative profiles respectively. The upper panel shows the case without Sommerfeld enhancement and the lower one the near-resonance case with a $\sigma_{\rm vel}$-dependent boost factor ($S_{\rm max} \sim 10^6$) as described in section III.

Looking at the cumulative distribution in Fig. 7, we see that at the virial radius, r_{200}, the ratio of the total intra-stream luminosity to the total smooth luminosity is $\sim 10^{-3}$ in the

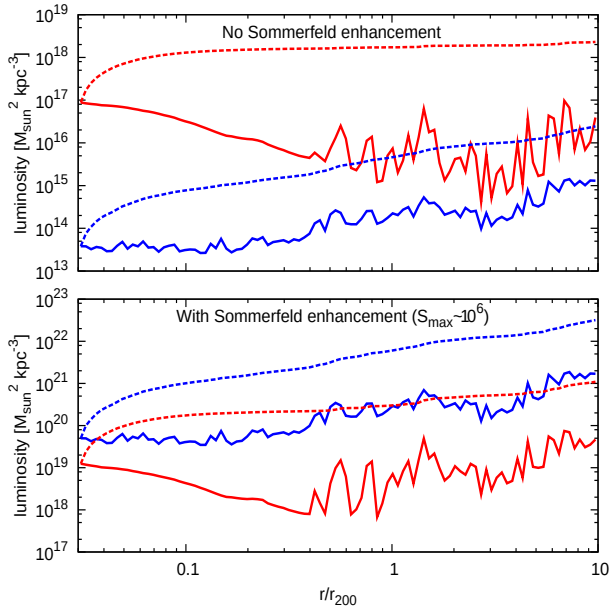

FIG. 7: Differential (solid) and cumulative (dashed) radial profiles of the annihilation luminosity for the smooth halo component (red) and for the streams component (blue) for the cases with and without Sommerfeld enhancement in the lower and upper panels respectively. The former, is for the near-resonance case described in section III that has a saturation value of $S_{\rm max} \sim 10^6$.

case with no enhancement. This ratio increases to ~ 20 once the extreme case of near-resonance enhancement is included. Thus, due to the low velocity dispersion of dark matter particles in streams, the annihilation rate in streams dominates over the rate given by the smooth mean density contribution. This contribution from streams remains nevertheless significantly smaller than the subhalo contribution. Considering subhalos with masses down to $10^{-6}{\rm M}_\odot$, the ratio of the total subhalo to smooth luminosity for MW-like halos lies in the range: $2 - 2 \times 10^3$ for the case without Sommerfeld enhancement and $4 \times 10^3 - 7 \times 10^6$ for the near-resonance case (see section C 2 b). The subhalo contribution is at least 1000 times larger than the stream contribution when the annihilation cross section is not enhanced by a Sommerfeld mechanism. Once the latter is included, it boosts all components (smooth, subhalos and streams) accordingly by a factor which is bounded by $S_{\rm max}$. Because the subhalo contribution is dominated by the smallest unresolved subhalos and these are essentially in the saturated regime, they are boosted by the same amount as the streams, and thus prevail as the dominant component of the annihilation luminosity in a halo.

[1] F. D. Steffen, European Physical Journal C **59**, 557 (2009), 0811.3347.
[2] J. L. Feng, ARA&A **48**, 495 (2010), 1003.0904.
[3] O. Adriani, G. C. Barbarino, G. A. Bazilevskaya, and et al., Nature **458**, 607 (2009), 0810.4995.
[4] D. Hooper, P. Blasi, and P. Dario Serpico, Journal of Cosmology and Astro-Particle Physics **1**, 25 (2009), 0810.1527.
[5] Y. Fujita, K. Kohri, R. Yamazaki, and K. Ioka, Phys. Rev. D **80**, 063003 (2009), 0903.5298.
[6] L. Bergström, J. Edsjö, and G. Zaharijas, Physical Review Letters **103**, 031103 (2009), 0905.0333.
[7] J. Lavalle, Q. Yuan, D. Maurin, and X. Bi, A&A **479**, 427 (2008), 0709.3634.
[8] M. Vogelsberger, S. D. M. White, R. Mohayaee, and V. Springel, MNRAS **400**, 2174 (2009), 0906.4341.
[9] M. Vogelsberger and S. D. M. White, MNRAS Online Early (2011), 1002.3162.
[10] J. Hisano, S. Matsumoto, and M. M. Nojiri, Physical Review Letters **92**, 031303 (2004), arXiv:hep-ph/0307216.
[11] N. Arkani-Hamed, D. P. Finkbeiner, T. R. Slatyer, and N. Weiner, Phys. Rev. D **79**, 015014 (2009), 0810.0713.
[12] M. Lattanzi and J. Silk, Phys. Rev. D **79**, 083523 (2009), 0812.0360.
[13] S. Galli, F. Iocco, G. Bertone, and A. Melchiorri, Phys. Rev. D **80**, 023505 (2009), 0905.0003.
[14] T. R. Slatyer, N. Padmanabhan, and D. P. Finkbeiner, Phys. Rev. D **80**, 043526 (2009), 0906.1197.
[15] G. Hütsi, J. Chluba, A. Hektor, and M. Raidal (2011), 1103.2766.
[16] J. B. Dent, S. Dutta, and R. J. Scherrer, Physics Letters B **687**, 275 (2010), 0909.4128.
[17] J. Zavala, M. Vogelsberger, and S. D. M. White, Phys. Rev. D **81**, 083502 (2010), 0910.5221.
[18] S. Hannestad and T. Tram, Journal of Cosmology and Astro-Particle Physics **1**, 16 (2011), 1008.1511.
[19] D. P. Finkbeiner, L. Goodenough, T. R. Slatyer, M. Vogelsberger, and N. Weiner (2010), 1011.3082.
[20] P. Ullio, L. Bergström, J. Edsjö, and C. Lacey, Phys. Rev. D **66**, 123502 (2002), arXiv:astro-ph/0207125.
[21] J. E. Taylor and J. Silk, MNRAS **339**, 505 (2003), arXiv:astro-ph/0207299.
[22] D. Elsässer and K. Mannheim, Physical Review Letters **94**, 171302 (2005), arXiv:astro-ph/0405235.
[23] S. Ando and E. Komatsu, Phys. Rev. D **73**, 023521 (2006), arXiv:astro-ph/0512217.
[24] A. Cuoco, S. Hannestad, T. Haugbølle, G. Miele, P. D. Serpico, and H. Tu, Journal of Cosmology and Astro-Particle Physics **4**, 13 (2007), arXiv:astro-ph/0612559.
[25] W. de Boer, A. Nordt, C. Sander, and V. Zhukov, A&A **470**, 61 (2007), 0705.0094.
[26] A. Cuoco, J. Brandbyge, S. Hannestad, T. Haugbølle, and G. Miele, Phys. Rev. D **77**, 123518 (2008), 0710.4136.
[27] M. Fornasa, L. Pieri, G. Bertone, and E. Branchini, Phys. Rev. D **80**, 023518 (2009), 0901.2921.
[28] J. M. Siegal-Gaskins and V. Pavlidou, Physical Review Letters **102**, 241301 (2009), 0901.3776.
[29] S. Profumo and T. E. Jeltema, Journal of Cosmology and Astro-Particle Physics **7**, 20 (2009), 0906.0001.
[30] A. V. Belikov and D. Hooper, Phys. Rev. D **81**, 043505 (2010), 0906.2251.

[31] G. Hütsi, A. Hektor, and M. Raidal, Journal of Cosmology and Astroparticle Physics **7**, 8 (2010), 1004.2036.

[32] M. Ajello, J. Greiner, G. Sato, D. R. Willis, G. Kanbach, A. W. Strong, R. Diehl, G. Hasinger, N. Gehrels, C. B. Markwardt, et al., ApJ **689**, 666 (2008), 0808.3377.

[33] R. C. Hickox and M. Markevitch, ApJ **661**, L117 (2007), arXiv:astro-ph/0702556.

[34] A. A. Abdo, M. Ackermann, M. Ajello, and et al., ApJ **720**, 435 (2010).

[35] S. Ando and V. Pavlidou, MNRAS **400**, 2122 (2009), 0908.3890.

[36] J. Zavala, V. Springel, and M. Boylan-Kolchin, MNRAS **405**, 593 (2010), 0908.2428.

[37] M. Boylan-Kolchin, V. Springel, S. D. M. White, A. Jenkins, and G. Lemson, MNRAS **398**, 1150 (2009), 0903.3041.

[38] S. Colafrancesco, S. Profumo, and P. Ullio, A&A **455**, 21 (2006), arXiv:astro-ph/0507575.

[39] N. Padmanabhan and D. P. Finkbeiner, Phys. Rev. D **72**, 023508 (2005), arXiv:astro-ph/0503486.

[40] J. Hisano, S. Matsumoto, M. M. Nojiri, and O. Saito, Phys. Rev. D **71**, 063528 (2005), arXiv:hep-ph/0412403.

[41] J. Bovy, Phys. Rev. D **79**, 083539 (2009), 0903.0413.

[42] V. Springel, S. D. M. White, C. S. Frenk, J. F. Navarro, A. Jenkins, M. Vogelsberger, J. Wang, A. Ludlow, and A. Helmi, Nature **456**, 73 (2008), 0809.0894.

[43] P. Gondolo, J. Edsjö, P. Ullio, L. Bergström, M. Schelke, and E. A. Baltz, Journal of Cosmology and Astro-Particle Physics **7**, 8 (2004), arXiv:astro-ph/0406204.

[44] P. Gondolo, J. Edsjö, P. Ullio, L. Bergstrom, M. Schelke, and E. A. Baltz, New Astronomy Review **49**, 149 (2005).

[45] H. Baer, F. E. Paige, S. D. Protopescu, and X. Tata, ArXiv High Energy Physics - Phenomenology e-prints (2003), arXiv:hep-ph/0312045.

[46] A. Moretti, C. Pagani, G. Cusumano, S. Campana, M. Perri, A. Abbey, M. Ajello, A. P. Beardmore, D. Burrows, G. Chincarini, et al., A&A **493**, 501 (2009).

[47] E. Churazov, R. Sunyaev, M. Revnivtsev, S. Sazonov, S. Molkov, S. Grebenev, C. Winkler, A. Parmar, A. Bazzano, M. Falanga, et al., A&A **467**, 529 (2007), arXiv:astro-ph/0608250.

[48] E. Treister, C. M. Urry, and S. Virani, ApJ **696**, 110 (2009), 0902.0608.

[49] K. Watanabe, D. H. Hartmann, M. D. Leising, L. The, G. H. Share, and R. L. Kinzer, in *Proceedings of the Fourth Compton Symposium*, edited by C. D. Dermer, M. S. Strickman, & J. D. Kurfess (1997), vol. 410 of *American Institute of Physics Conference Series*, pp. 1223–1227.

[50] G. Weidenspointner, M. Varendorff, S. C. Kappadath, and et al., in *American Institute of Physics Conference Series*, edited by M. L. McConnell & J. M. Ryan (2000), vol. 510 of *American Institute of Physics Conference Series*, pp. 467–470.

[51] A. W. Strong, I. V. Moskalenko, and O. Reimer, ApJ **613**, 956 (2004), arXiv:astro-ph/0405441.

[52] A. A. Abdo, M. Ackermann, M. Ajello, and et al., Journal of Cosmology and Astroparticle Physics **4**, 14 (2010).

[53] R. C. Hickox and M. Markevitch, ApJ **645**, 95 (2006), arXiv:astro-ph/0512542.

[54] M. Ajello, L. Costamante, R. M. Sambruna, N. Gehrels, J. Chiang, A. Rau, A. Escala, J. Greiner, J. Tueller, J. V. Wall, et al., ApJ **699**, 603 (2009), 0905.0472.

[55] Y. Inoue, T. Totani, S. Inoue, M. A. R. Kobayashi, J. Kataoka, and R. Sato, ArXiv e-prints (2010), 1001.0103.

[56] B. D. Fields, V. Pavlidou, and T. Prodanović, ApJ **722**, L199 (2010), 1003.3647.

[57] M. Kamionkowski, S. M. Koushiappas, and M. Kuhlen, Phys. Rev. **D81**, 043532 (2010), 1001.3144.

[58] A. A. Abdo, M. Ackermann, M. Ajello, and et al., Physical Review Letters **104**, 101101 (2010), 1002.3603.

[59] J. L. Feng, M. Kaplinghat, and H.-B. Yu, Phys. Rev. **D82**, 083525 (2010), 1005.4678.

[60] T. Bringmann, New J. Phys. **11**, 105027 (2009), 0903.0189.

[61] A. Loeb and N. Weiner (2010), 1011.6374.

[62] N. F. Bell, A. J. Galea, and K. Petraki, Phys. Rev. **D82**, 023514 (2010), 1004.1008.

[63] J. L. Feng and D. Sanford, ArXiv e-prints (2010), 1009.3934.

[64] R. Essig, N. Sehgal, L. E. Strigari, M. Geha, and J. D. Simon, Phys. Rev. D **82**, 123503 (2010), 1007.4199.

[65] R. Schlickeiser, *Cosmic Ray Astrophysics* (2002).

[66] C. L. Carilli and G. B. Taylor, ARA&A **40**, 319 (2002), arXiv:astro-ph/0110655.

[67] P. P. Kronberg, R. Kothes, C. J. Salter, and P. Perillat, ApJ **659**, 267 (2007), 0704.3288.

[68] C. Longair, Astronomische Nachrichten **317**, 156 (1996).

[69] S. Redfield and R. E. Falcon, ApJ **683**, 207 (2008).

[70] S. Colafrancesco, S. Profumo, and P. Ullio, Phys. Rev. D **75**, 023513 (2007), arXiv:astro-ph/0607073.

[71] R. C. Gilmore, P. Madau, J. R. Primack, R. S. Somerville, and F. Haardt, MNRAS **399**, 1694 (2009), 0905.1144.

[72] J. F. Navarro, C. S. Frenk, and S. D. M. White, ApJ **490**, 493 (1997), arXiv:astro-ph/9611107.

[73] V. Springel, J. Wang, M. Vogelsberger, A. Ludlow, A. Jenkins, A. Helmi, J. F. Navarro, C. S. Frenk, and S. D. M. White, MNRAS **391**, 1685 (2008), 0809.0898.

[74] J. March-Russell and S. M. West, Physics Letters B **676**, 133 (2009), 0812.0559.

[75] W. Shepherd, T. M. P. Tait, and G. Zaharijas, Phys. Rev. D **79**, 055022 (2009), 0901.2125.

[76] J. F. Navarro, A. Ludlow, V. Springel, J. Wang, M. Vogelsberger, S. D. M. White, A. Jenkins, C. S. Frenk, and A. Helmi, MNRAS **402**, 21 (2010), 0810.1522.

[77] Here $\mathcal{E}_{\rm e}$ is the local electron (and positron) emissivity, analogous to the photon emissivity defined in Eq. (1).

[78] The related phenomenon of radiative capture into WIMPonium, allowed for $m_\phi < \alpha_{\rm c}^2 m_\chi/4$, can increase the effective enhancement factor substantially for small m_ϕ [74, 75].

[79] Unless otherwise stated, velocities are given in units of the speed of light c.

[80] The equilibrium spectrum as defined in Eq. (4) was scaled by a factor of 10^{-16} to show it in the same figure.

[81] Although the formalism required to compute the enhancement is more complicated than the one given in section III, which is strictly valid for scalar boson carriers, the results are qualitatively similar [12].

[82] Specifically, we take the obscured and unobscured Compton-thin AGN contributions to the signal in this energy range (red and blue solid lines in Fig. 5 of [48]). We do not include the contribution from Compton-thick AGN that has a more uncertain modeling. We note that due to this, upper limits to the contribution of sources other than AGN in this energy range are expected to be lower than those shown in Fig. 2.

[83] Here we have changed the comoving distance r in Eq. (2) for the redshift z and use the mean value theorem of integral calculus, which can be used because the remainder integrand in Eq. (12) is always positive in the interval of integration.

[84] A web application that computes the Sommerfeld enhancement for this type of models is located at http://astrometry.fas.harvard.edu/mvogelsb/sommerfeld/ (see the last paragraph of the Conclusions in [19] for a description).

[85] Additional backgrounds such as starlight, infrared and ultraviolet contribute as well, but we have neglected them since the CMB is by far the largest of these background populations.

[86] An Einasto profile seems to be favored over a NFW by the most recent high-resolution N-body simulations (e.g. [76]), using the former instead of the latter increases the net annihilation rate in a halo by only 50% [36]. This effect is small compared to other uncertainties in our analysis.

[87] At z=0, $\sigma_{\rm vel} \propto M_{\rm v}^{0.34}$